

 Open access • Posted Content • DOI:10.1101/2020.06.03.132654

Chromatin remodeler Brahma safeguards canalization in cardiac mesoderm differentiation — [Source link](#)

Swetansu K. Hota, [Swetansu K. Hota](#), [Andrew P. Blair](#), [Kavitha S. Rao](#) ...+8 more authors

Institutions: [University of California, Berkeley](#), [Gladstone Institutes](#), [University of California, San Francisco](#)

Published on: 04 Jun 2020 - [bioRxiv](#) (Cold Spring Harbor Laboratory)

Topics: [Mesoderm](#), [Germ layer](#), [Chromatin remodeling](#) and [Chromatin](#)

Related papers:

- [p53 Coordinates Temporal WDR5 Inputs During Neuroectoderm and Mesoderm Differentiation of Mouse Embryonic Stem Cells](#)
- [Sox2 and canonical Wnt signaling interact to activate a developmental checkpoint coordinating morphogenesis with mesodermal fate acquisition](#)
- [Role of Cdx factors in early mesodermal fate decisions](#)
- [Cell cycle regulators control mesoderm specification in human pluripotent stem cells](#)
- [The Essential Roles of the Chromatin Factor Gon4l in Heart Development](#)

Share this paper:    

View more about this paper here: <https://typeset.io/papers/chromatin-remodeler-brahma-safeguards-canalization-in-52o3zs6ouj>

1 Chromatin remodeler Brahma safeguards canalization in cardiac mesoderm differentiation

2

3 Swetansu K. Hota^{1,2,3}, Andrew P. Blair¹, Kavitha S. Rao^{1,2}, Kevin So^{1,2}, Aaron M. Blotnick^{1,2},

4 Ravi V. Desai¹, Leor S. Weinberger^{1,5,6}, Irfan S. Kathiriya^{1,2,4}, and Benoit G. Bruneau^{1,2,3,7}

5

6 1. Gladstone Institutes, San Francisco, CA, 94158 USA

7 2. Roddenberry Center for Stem Cell Biology and Medicine at Gladstone, San Francisco, CA

8 94158, USA

9 3. Cardiovascular Research Institute, University of California, San Francisco, CA 94158 USA

10 4. Department of Anesthesia and Perioperative Care, University of California, San Francisco,

11 San Francisco, CA 94158, USA

12 5. Department of Pharmaceutical Chemistry, University of California, San Francisco, CA 94158,

13 USA

14 6. Department of Biochemistry and Biophysics, University of California, San Francisco, CA

15 94158, USA

16 7. Department of Pediatrics, University of California, San Francisco, San Francisco, CA 94143

17 USA

18

19 Correspondence to B.G.B. (benoit.bruneau@gladstone.ucsf.edu); S.K.H

20 (swetansu.hota@gladstone.ucsf.edu)

21

22 SUMMARY

23 Differentiation proceeds along a continuum of increasingly fate-restricted intermediates, referred

24 to as canalization¹⁻⁴. Canalization is essential for stabilizing cell fate, but the mechanisms

25 underlying robust canalization are unclear. Here we show that deletion of the BRG1/BRM-

26 associated factor (BAF) chromatin remodeling complex ATPase gene *Brm* (encoding Brahma)
27 results in a radical identity switch during directed cardiogenesis of mouse embryonic stem cells
28 (ESCs). Despite establishment of well-differentiated precardiac mesoderm, *Brm*-null cells
29 subsequently shifted identities, predominantly becoming neural precursors, violating germ layer
30 assignment. Trajectory inference showed sudden acquisition of non-mesodermal identity in
31 *Brm*-null cells, consistent with a new transition state inducing a fate switch referred to as a
32 saddle-node bifurcation^{3,4}. Mechanistically, loss of *Brm* prevented de novo accessibility of
33 cardiac enhancers while increasing expression of the neurogenic factor POU3F1 and preventing
34 expression of the neural suppressor REST. *Brm* mutant identity switch was overcome by
35 increasing BMP4 levels during mesoderm induction, repressing *Pou3f1* and re-establishing a
36 cardiogenic chromatin landscape. Our results reveal BRM as a compensable safeguard for
37 fidelity of mesoderm chromatin states, and support a model in which developmental canalization
38 is not a rigid irreversible path, but a highly plastic trajectory that must be safeguarded, with
39 implications in development and disease.

40

41 (Main Text)

42 Our previous studies indicated the prevalence of BRM in the cardiomyocyte-enriched chromatin
43 remodeling complex BAF170⁵. BRM has been reported to be dispensable for mouse
44 development⁶, but it is implicated in human developmental syndromes^{7,8}, mouse skeletal muscle
45 function⁹, and several cancers^{10,11}, and can partly compensate for loss of BRG1¹²⁻¹⁶. To
46 determine the role of BRM in cardiac differentiation, we deleted *Brm* in ESCs and directed
47 cardiac differentiation (Fig. 1a, Extended data Fig. 1a). *Brm*^{-/-} cells failed to generate beating
48 cTnT+ cardiomyocytes (Extended Data movies. 1-3) and as measured by immunofluorescence
49 (Fig. 1b) and flow cytometry (Fig. 1c). This was confirmed in three independent *Brm*^{-/-} lines,
50 while two heterozygous lines from the same set of clones differentiated well. RNA-seq during

51 the differentiation time course showed that at D4, mesoderm gene expression was unaffected in
52 *Brm*^{-/-} cells, while D6 (cardiac precursor, CP) and D10 (cardiomyocyte, CM) gene expression
53 was significantly altered (FDR<0.05, \pm 2-fold change) (Extended data Fig. 1b, c). At D6, several
54 important cardiac TFs were not induced in *Brm*^{-/-} cells (*Isl1*, *Hand2*, *Nkx2-5*, *Mef2c*, *Tbx20*),
55 whereas osteoblast- and neural-associated TFs were upregulated (*Tcf15*, *Sox2*). At D10, when
56 WT cells had reached the beating cardiomyocyte stage, *Brm*^{-/-} cells completely failed to activate
57 cardiac genes and instead expressed genes associated with neural (*Ascl1*, *Pax6*, *Neurod1*,
58 *Neurog1*, *Olig2* and *Sox2*) or other (e.g. erythrocyte *Gata1*, *Tal1*) cell types (Fig. 1d).

59

60 **BRM safeguards CP differentiation to CM and represses neural and other gene programs**

61 The drastic gene expression changes in *Brm*^{-/-} cells upon cardiac differentiation suggested
62 either 1) the formation of new non-cardiac populations or 2) that a relatively homogeneous
63 population activated normally mutually-exclusive expression modules. To differentiate between
64 these scenarios, we performed single cell RNA-seq on 21,991 WT and *Brm*^{-/-} cells at D10 of
65 differentiation using the 10X Genomics dropseq platform. Uniform Manifold Approximation and
66 Projections (UMAP)¹⁷ plots showed that *Brm*^{-/-} cells at D10 were radically distinct from their WT
67 counterparts (Fig. 1e), lacked expression of cardiac genes, and clustered in multiple sub-
68 populations. These included cells with signatures of neural stem cells (*Sox2*, *Sox9*, *Neurod1*,
69 *and Ascl1*), neural progenitors or immature neurons (*Dcx*, *Otx2*, *Gap43*, *Tubb2b*, *Tubb3*), glial
70 (*Gfap*, *Olig2*) and Schwann cells (*Gap43*), and retinal neuronal precursors (*Rax*, *Lhx2*, *Lmo1*)
71 (Figs. 1f, g, Extended Data Fig. 1d). We also identified a cluster of cells expressing markers of
72 osteoblast development (*Postn*, *Bgn*, *Col1a1*, *Fbn2*, *Twist2*), indicating that some *Brm*^{-/-} cells
73 adopt non-cardiac mesodermal fates. Immunofluorescence showed TUBB3+ staining in D10
74 *Brm*^{-/-} cells, displaying neuron like outgrowths (Fig. 1h). Notably, no other mesodermal or
75 ectodermal derivatives, nor endodermal cell types, were observed, indicating that BRM deletion

76 induced a specific fate switch. Loss of BRM did not seem to affect directed neuronal precursor
77 differentiation (Extended Data Fig. 1e).

78

79 **BRM controls the mesoderm to cardiac precursor transition**

80 To elucidate the events underlying the anomalous differentiation in absence of BRM, we
81 examined the time courses of differentiation of WT and *Brm*^{-/-} cells by single cell RNA-seq (Fig.
82 2a). Consistent with bulk RNA-seq, D4 (mesoderm) *Brm*^{-/-} cells were statistically similar to WT
83 cells and both occupied the same UMAP space (Fig. 2b-d). *Brm*^{-/-} cells segregated slightly
84 based on modest (less than 2-fold) changes in expression of a few genes (*Mesp1*, *Lhx1*, *Fn1*,
85 *Rps28*) (Supplementary Sheet 1). In sharp contrast, at D6 *Brm*^{-/-} clustered separately from WT
86 cells (Fig. 2b). Most D6 WT cells expressed well-defined CP markers (*Smarcd3*, *Mef2c*, *Hand2*;
87 Fig. 2d, Extended Data Fig. 2a), whereas *Brm*^{-/-} cells mostly expressed genes involved in neural
88 lineages (*Gbx2*, *Sox2*, *Irx3*, *Crabp1*, *Crabp2* and *Prtg*; Fig. 2d, Extended Data Fig. 2a). The few
89 D6 WT and *Brm*^{-/-} cells that clustered together expressed markers of hematopoietic lineages
90 (*Gata1*, *Klf1*, *Hbb1*; Supplementary Sheet 2), suggesting a low level of BRM-independent
91 hematopoietic differentiation. As expected, D10 WT and *Brm*^{-/-} cells clustered largely in different
92 UMAP space (Fig. 2b-d). Our time course therefore indicates a crucial early role of BRM
93 immediately following cardiac mesoderm formation. Partition Based Graph Abstraction¹⁸
94 revealed genotype-dependent connectivity (Fig. 2e-g). WT and *Brm*^{-/-} cells at D4 predominantly
95 connected with their respective D6 and D10 genotype-specific clusters. A small percentage of
96 WT and *Brm*^{-/-} D6 cells connected to clusters 5 and 12 forming hematopoietic and endothelial
97 clusters (Fig. 2e-g). To further assess the differentiation paths, we built differentiation
98 trajectories in the form of a branching tree using URD¹⁹. *Pou5f1*⁺ -WT and *Brm*^{-/-} clusters were
99 selected as the root, while D10 clusters were defined as tips. Only WT cells progressed in

100 stepwise pseudotime to CPs and their derivatives. In contrast, *Brm*^{-/-} cells directly transitioned
101 from mesoderm to non-cardiac neural lineages after D4 (Fig. 2h, i, Extended Data Fig. 2b, c) .
102
103 Quantitative gene expression analysis at D4 revealed minimal expression of pluripotency
104 (*Nanog* and *Sox2*) and paraxial mesoderm markers (*Tbx6*, *Msgn1*), while primitive streak
105 marker (*T*) and mesoderm precursor (*Pou5f1* or *Oct4*) showed minimal changes between
106 genotypes (Extended Data Fig. 2a), confirming proper cardiogenic mesoderm differentiation of
107 *Brm*^{-/-} cells. The absence of *Tbx6*⁺/*Sox2*⁺ or *T*⁺/*Sox2*⁺ cells precluded the possibility that *Brm*^{-/-}
108 cells represent neuromesodermal precursors, especially given that our differentiation lacks
109 retinoic acid^{20,21}. At D4, we did not observe transcriptional changes in neuroectodermal
110 markers²² between WT and *Brm*^{-/-} cells. Indeed, the continuous expression of POU5F1 and
111 absence of SOX2 indicated that D4 cells are derived from a mesendoderm rather than an
112 neuroectoderm lineage^{23,24}, suggesting *Brm*^{-/-} cells acquire neural lineage after D4 (Fig. 2c,
113 Extended Data Fig. 2a).
114
115 BRG1, a paralog of BRM, has important roles in cardiogenesis^{5,25,26}. To compare the role of
116 *Brg1* to that of *Brm* in cardiac differentiation, we induced genetic *Brg1* deletion^{25,27} at D2 and
117 analyzed the effects at D4 and D10 by single cell RNA-seq (Extended Data Fig. 3a). *Brg1* loss
118 did not affect D4 transcription broadly (Extended Data Fig. 3b, c). However, at D10, WT and
119 *Brg1* KO cells clustered separately (Extended Data Fig. 3b). Marker analysis revealed that
120 *Brg1*-deficient cells formed very few cardiac myocytes and instead formed endothelial cells,
121 fibroblasts, neural progenitors, and developmentally-arrested progenitors (Extended Data Fig.
122 3b-e). Unlike *Brm*^{-/-} cells, we did not observe TUBB3 staining in *Brg1* KO cells (Extended Data
123 Fig. 3f).
124

125 These results show that under directed differentiation conditions, *Brm*^{-/-} cells form specified
126 cardiac mesodermal cells, however then undergo a radical fate change towards a constellation
127 of non-cardiac, largely neuronal cell types. Loss of Brg1 also had a similar but less severe
128 phenotype, indicating essential but distinct roles of BAF complex ATPases in regulating
129 lineages during differentiation^{28,29}.

130

131 **BRM modulates dynamic chromatin accessibility**

132 We next used ATAC-seq³⁰ to examine BRM's role in modulating chromatin accessibility during
133 cardiac differentiation (Fig. 3a). Although gene expression was minimally affected at D4, we
134 found significant changes (FDR<0.05, fold change >2) at 3320 chromatin regions, 98.3% of
135 which showed reduced accessibility upon *Brm* loss. These sites were enriched for genes
136 involved in cardiac and other developmental pathways (Fig. 3b). At D6 and D10 8814 and 5391
137 regions were significantly changed (FDR<0.05, fold change >2), respectively, between
138 genotypes (Supplementary Sheet 3). Consistent with the RNA-seq data, at D6 the differentially
139 closed chromatin in *Brm*^{-/-} cells was near regulatory elements of cardiac development genes,
140 including TFs such as *Gata4*, *Tbx5*, *Nkx2-5*, *Myocd*, *Hand2*, *Mef2c*, and cardiac functional
141 genes such as *Ttn*, *Myh2*, *Myh6*, *Myh7*, *Actc1*. In contrast, D6 *Brm*^{-/-} cells had newly open
142 chromatin near genes involved in non-cardiac differentiation processes, including some neural
143 genes (e.g. *Pax6*) (Fig. 3c), consistent with initiation of neural gene expression. By D10, a clear
144 and strong association was found with accessible chromatin near neural differentiation-related
145 genes (Fig. 3d). Comparison of temporal accessibility patterns for select genes revealed that
146 BRM maintains accessibility near cardiac genes throughout differentiation beginning at D4 (Fig.
147 3e, Extended Data Fig. 4a). In contrast, loss of BRM induced or maintained accessibility near
148 neural genes at or after D6 (Fig. 3e, extended Data Fig. 4b).

149

150 Altered chromatin accessibility was highly correlated with gene expression changes at D6 and
151 D10 (Figs. 3f and 3g). Comparing BRM-mediated chromatin accessibility to active enhancers
152 identified by H3K27ac marks^{31,32} showed that BRM promoted accessible regions at CP and CM
153 enhancers (Figs. 3h and 3i). Conversely, BRM-mediated closed chromatin associated
154 significantly with neural progenitor enhancers in CMs³². Motifs enriched in ATAC-seq peaks that
155 were significantly depleted in *Brm*^{-/-} included those for cardiac-related transcription factors
156 (GATA4, MEF2C, HAND2) while peaks newly opened in absence of BRM were enriched for
157 motifs for neuronal TFs (SOX2, OCT6/8 (POU3F1/3), OTX2, LHX2/3, RFX; Extended Data Fig.
158 4c). Thus, BRM promotes open chromatin at cardiogenic genes, while subsequently
159 establishing or maintaining the inaccessible state of non-cardiac (including neural) enhancers.

160

161 **Timing of BRM function**

162 To more precisely pinpoint the timing of BRM function, we created an auxin-inducible degron ES
163 cell line³³ to rapidly deplete BRM (Extended Fig. 4d). Continuous auxin application largely
164 recapitulated the impaired cardiac differentiation of *Brm*^{-/-} cells, with a low level of remaining
165 TNNT2+ cells likely due to incomplete BRM depletion in a proportion of cells (Extended Data
166 Fig. 4e)³³. Depletion of BRM prior to D4 impaired differentiation, whereas subsequent depletion
167 did not greatly affect global cardiac differentiation (Extended Data Fig. 4f). BRM loss did not
168 affect ESC pluripotency or self-renewal (Extended Data Fig. 5a). These results indicate a critical
169 role for BRM after exit from pluripotency, and during cardiac mesoderm formation, but before
170 mesoderm to CP transition.

171

172 **Epigenetic regulation of chromatin by BRM**

173 BAF complex subunits been implicated in modulation of chromatin in lineage-specific
174 enhancers^{25,34}. BRM specifically facilitates acetylation of H3K27 residues at H3K27me3

175 enriched Polycomb targets^{35,36}. To understand if BRM modulates enhancer landscape via
176 histone modifications, we profiled the effect of BRM loss on H3K27ac and H3K27me marks. At
177 D4 of cardiac differentiation, very few regions were differentially enriched with H3K27me3. At
178 later stages, regions near cardiovascular genes gained H3K27me3 marks upon BRM loss, while
179 PcG-repressed genes involved in early embryo development lost their H3K27me3 marks
180 (Extended Data Fig. 6a).

181
182 Conversely, in D6 and D10 *Brm*^{-/-} cells, H3K27ac was reduced near genes associated with
183 cardiac muscle development and contraction (Fig. 4a, clusters *c* and *f*, Extended Data Fig. 5c,d,
184 6c,d), and increased near genes involved in cell fate specification, neurogenesis and regulation
185 of neuron differentiation (Fig. 4a, clusters *a*, *g* and *l*, Extended Data Fig. 5c, d, 6c,d),
186 concordant with ATACseq data. Sites reduced in *Brm*^{-/-} cells were enriched for cardiac TFs,
187 while sites that gained H3K27ac marks were enriched for neural TF motifs (Extended Data Fig.
188 5f, g). At D4, sites with reduced H3K27ac in *Brm*^{-/-} cells were enriched near cardiovascular
189 development genes (Fig. 4a, cluster *b*, Extended Data Fig 5b, e), and had motifs for cardiac
190 TFs. Despite the absence of accessibility changes we observed sites that gained H3K27ac in
191 D4 *Brm*^{-/-} cells, including genes involved in stem cell maintenance and neurogenesis (Fig. 4a,
192 cluster *h*), which were enriched for POU or OCT motifs (Fig. 4b).

193
194 The enrichment of POU motifs suggested a potential involvement of these TFs in neural
195 induction in *Brm*^{-/-} cells. Bulk RNAseq with lower statistical cutoff (raw p-value <0.05) showed a
196 modest increase in *Pou3f1* (*Oct6*) mRNA in *Brm*^{-/-} D4 cells; other POU factors were not
197 detected. POU3F1 promotes neural fate by activating neural lineage genes and inhibiting
198 BMP4-dependent transcription³⁷. We found that POU3F1 protein was expressed at D2, and
199 thereafter reduced during WT differentiation (Fig. 4c). Despite the low level of mRNA induction,

200 POU3F1 protein was robustly increased at D4 and D6 in *Brm*^{-/-} cells (Fig. 4c), suggesting
201 prolonged POU3F1 may initiate the neurogenic gene expression program. Indeed, knockdown
202 of *Pou3f1* in *Brm*^{-/-} cells resulted in fewer TUBB3⁺ neuronal progenitor cells and absence of
203 filamentous extensions (Fig. 4d).

204

205 To delineate BRM occupancy, we performed chromatin immunoprecipitation followed by
206 sequencing (ChIP-seq) using anti-FLAG antibody on a BRM-3xFLAG tagged strain at D4, D6
207 and D10 (Extended Data Fig. 7a). BRM bound to 110 regions at D4, 521 regions at D6 and
208 1188 regions at D10 (Extended Data Fig. 7b-d and Supplementary Sheet 4), consistent with its
209 increasing expression pattern during cardiac differentiation. BRM-bound regions were enriched
210 for genes involved in transcriptional and post-transcriptional regulation of gene expression at D4
211 and D6, and for regulation of muscle development at D10 (Extended Data Fig. 7e). Motif
212 analysis revealed enrichment of REST motifs at all stages, along with cardiac TFs at D10 (Fig.
213 4e). Moreover, BRM deletion abrogated REST expression at D10 (Fig. 4f). REST knockdown
214 from D4 to D7 resulted in ectopic expression of TUBB3⁺ cells at D10 (Fig. 4g), suggesting BRM
215 controls expression of REST to specifically represses neural lineage genes during cardiac
216 differentiation.

217

218 **Signal-dependent rescue of anomalous differentiation**

219 The BRM degron experiments suggested that BRM is most critical during cardiac mesoderm
220 induction (Extended Data Fig. 4f). At this stage, BRM regulates neuronal lineage inducing factor
221 POU3F1, which can counteract BMP signaling³⁷. BMP4 concentration at this stage is finely
222 regulated to ensure proper cardiac differentiation^{38,39}. In our system, supraphysiological
223 exogenous BMP4 concentration inhibited cardiac differentiation of WT ESCs but rescued
224 cardiac differentiation of *Brm*^{-/-} ESCs (Fig 5a, Extended Data Fig. 8a). High BMP4 also

225 repressed prolonged POU3F1 expression in *Brm*^{-/-} cells and normalized expression of BAF60c
226 and REST (Fig. 5b). Loss of BRG1, however was not similarly compensable by increasing
227 BMP4 concentrations (Extended Data Fig 8b).

228

229 BMP4-mediated BRM rescue restored accessibility of cardiac enhancers (Fig. 5c-e, Extended
230 Data Fig. 8c-e, see boxed regions and 8f). Conversely, neural progenitor enhancers were
231 inaccessible in *Brm*^{-/-} cells with high BMP4 (Fig. 5e, Extended Data Fig. 8g).

232

233 Single cell RNAseq analyses revealed BMP4-dependent changes in gene expression. At D4,
234 WT and *Brm*^{-/-} cells differentiated with normal BMP4 concentrations (3.2 ng/μl) clustered
235 together in the same UMAP space, but separated from the high BMP4 (12.8 ng/μl) samples
236 (Fig. 5f). Later in differentiation, high BMP4 WT cells clustered separately from normal BMP4-
237 treated cells, forming endothelial and hematopoietic progenitors, and eventually fibroblasts and
238 blood cells (Fig. 5f,g). As expected, *Brm*^{-/-} cells at normal BMP4 formed mostly neural progenitor
239 clusters (Fig. 5h) separate from WT cells. In contrast, *Brm*^{-/-} cells at high BMP4 clustered with
240 WT cells treated with normal BMP4 at D6 and D10, and expressed CP and CM markers (Figs.
241 5f, i, Extended Data Fig. 9a and Supplementary Sheet 5).

242

243 URD trajectory analysis with *Pou5f1*⁺ expressing clusters as root and D10 clusters as tips
244 placed WT and *Brm*^{-/-} cells at normal and high BMP4 concentrations at the trajectory root. At
245 normal BMP4, WT cells followed a step-wise trajectory forming cardiomyocytes, while *Brm*^{-/-}
246 cells followed a different path (Fig. 5j), however *Brm*^{-/-} cells at high BMP4 formed cardiac
247 progenitors and cardiomyocytes by following an almost identical trajectory to WT cells at normal

248 BMP4 (Fig. 5k, Extended Data Fig. 9b). Thus, simply modulating BMP4 signaling compensated
249 for the absence of BRM and completely restored the normal path of cardiac differentiation.

250

251 How BMP4 might change differentiation path of *Brm*^{-/-} cells is not clear. We confirmed that loss
252 of BRM simply did not change BMP4 availability to the cells (Extended Data Fig. 9c). BMP-
253 dependent gene regulatory networks are highly robust, and self-regulate in part by modulating
254 transcriptional noise^{40,41}. To evaluate if gene expression noise is regulated by BRM or BMP4,
255 we calculated cell-to-cell gene expression variability⁴² and single cell entropy⁴³ to predict
256 differentiation potential. At normal BMP4 both WT and *Brm*^{-/-} cells had similar dispersion and
257 entropy metrics, both of which increased in presence of high BMP4 at D4 (Extended Data Fig 9c
258 and 9d). This suggests increased intrinsic gene expression noise could participate in BMP4-
259 dependent modulation of the *Brm*^{-/-} transcriptional state.

260

261 **In vivo requirement for BRM**

262 *Brm*^{-/-} mice are viable, although the nature of the original allele has been questioned^{6,44}. Our
263 independent mouse line with an 8bp deletion at Exon 2 resulting a premature stop codon and
264 loss of BRM protein produced pups at Mendelian ratios (Extended Data Figs. 10a-c) confirming
265 viability of *Brm* knockout. Viability may be due to compensatory overexpression of BRG1 in *Brm*
266 knockout tissues (Extended Data Fig. 10d), which did not occur in our directed differentiation
267 system (Extended Data Fig. 10e).

268

269 **Discussion**

270 Along the “landscape” of cell fate decisions, epigenetic regulators are key determinants of
271 transition states. This is apparent in cancer, where new attractor states are formed that result in
272 anomalous differentiation or dedifferentiation. In normal development however, only scant

273 examples exist of natural transdifferentiation^{21,45,46}, pointing to stability and robustness of
274 canalization in vertebrate differentiation. Here we show that this stability during cardiac
275 differentiation requires safeguarding by BRM.
276
277 Artificially forced reprogramming overcomes cell states⁴⁷, and certain chromatin remodeling
278 factors including BRM are important safeguards against reprogramming⁴⁸⁻⁵¹. Conversely, other
279 BAF complex subunits (e.g. BRG1, BAF60c) enhance reprogramming⁵²⁻⁵⁴. Reprogramming of
280 fibroblasts to neurons involves transient competition between myogenic and neural gene
281 expression programs, evidence that genome plasticity can transcend germ layer specification⁵⁵.
282 It is likely that in the absence of BRM, deregulation of neurogenic TFs, e.g. POU3F1, activates a
283 cascade of neural gene expression in the context of broadly deregulated enhancer accessibility
284 (Fig. 5l). That we observe this “self-reprogramming” in a directed differentiation context, but not
285 in the complete organism indicates that the cues provided in vitro are strictly narrow parameters,
286 while in vivo they are likely highly buffered. Indeed, increased BRG1 in *Brm*^{-/-} mice and rescue of
287 *Brm*^{-/-} cells by elevated BMP signaling, indicates that loss of BRM is compensable.

288
289 Our findings indicate that BRM maintains developmental canalization of committed mesodermal
290 precursors by providing an epigenomic state that favors a limited range of transition states, and
291 that in its absence an unstable state induces a transition akin to a saddle node bifurcation (Fig.
292 5m). We highlight the fragility of the differentiation path, challenging the concept of highly robust
293 developmental canalization, with important implications for understanding the stability of gene
294 regulation in differentiation, and for deregulated gene expression in disease.

295

296

297

298 References

- 299 1. Waddington, C. H. Canalization of Development and the Inheritance of Acquired
300 Characters. *Nature* **150**, 563–565 (1942).
- 301 2. Waddington, C. H. *The Strategy of the Genes, a Discussion of Some Aspects of*
302 *Theoretical Biology, by C. H. Waddington,... With an Appendix [Some Physico-chemical*
303 *Aspects of Biological Organisation] by H. Kacser,...* (1957).
- 304 3. Ferrell, J. E., Jr. Bistability, Bifurcations, and Waddington's Review Epigenetic
305 Landscape. *Current Biology* **22**, R458–R466 (2012).
- 306 4. Moris, N., Pina, C. & Arias, A. M. Transition states and cell fate decisions in epigenetic
307 landscapes. *Nature Publishing Group* **17**, 693–703 (2016).
- 308 5. Hota, S. K. *et al.* Dynamic BAF chromatin remodeling complex subunit inclusion
309 promotes temporally distinct gene expression programs in cardiogenesis. *Development*
310 **146**, dev174086 (2019).
- 311 6. Reyes, J. C. *et al.* Altered control of cellular proliferation in the absence of mammalian
312 brahma (SNF2alpha). *The EMBO Journal* **17**, 6979–6991 (1998).
- 313 7. Van Houdt, J. K. J. *et al.* Heterozygous missense mutations in SMARCA2 cause
314 Nicolaides-Baraitser syndrome. *Nature Publishing Group* 1–6 (2012).
315 doi:10.1038/ng.1105
- 316 8. Tsurusaki, Y. *et al.* Mutations affecting components of the SWI/SNF complex cause
317 Coffin-Siris syndrome. *Nat Genet* **44**, 376–378 (2012).
- 318 9. Albin, S. *et al.* Brahma is required for cell cycle arrest and late muscle gene expression
319 during skeletal myogenesis. *EMBO reports* **16**, 1037–1050 (2015).
- 320 10. Wu, J. *et al.* Inactivation of SMARCA2 by promoter hypermethylation drives lung cancer
321 development. *Gene* **687**, 193–199 (2019).
- 322 11. Zhang, Z. *et al.* BRM/SMARCA2 promotes the proliferation and chemoresistance
323 of pancreatic cancer cells by targeting JAK2/STAT3 signaling. *Cancer Letters* **402**,
324 213–224 (2017).
- 325 12. Willis, M. S. *et al.* BRG1 and BRM function antagonistically with c-MYC in adult
326 cardiomyocytes to regulate conduction and contractility. *J. Mol. Cell. Cardiol.* **105**, 99–109
327 (2017).
- 328 13. Januario, T. *et al.* PRC2-mediated repression of SMARCA2 predicts EZH2 inhibitor
329 activity in SWI/SNF mutant tumors. *Proc. Natl. Acad. Sci. U.S.A.* **114**, 12249–12254
330 (2017).
- 331 14. Smith-Roe, S. L. & Bultman, S. J. Combined gene dosage requirement for SWI/SNF
332 catalytic subunits during early mammalian development. *Mamm. Genome* **24**, 21–29
333 (2013).
- 334 15. Hoffman, G. R. *et al.* Functional epigenetics approach identifies BRM/SMARCA2 as a
335 critical synthetic lethal target in BRG1-deficient cancers. *Proc. Natl. Acad. Sci. U.S.A.*
336 **111**, 3128–3133 (2014).
- 337 16. Wiley, M. M., Muthukumar, V., Griffin, T. M. & Griffin, C. T. SWI/SNF chromatin-
338 remodeling enzymes Brahma-related gene 1 (BRG1) and Brahma (BRM) are dispensable
339 in multiple models of postnatal angiogenesis but are required for vascular integrity in
340 infant mice. *J Am Heart Assoc* **4**, e001972–e001972 (2015).
- 341 17. McInnes, L., Healy, J. & Melville, J. UMAP: Uniform Manifold Approximation and
342 Projection for Dimension Reduction. *arXiv.org stat.ML*, arXiv:1802.03426 (2018).
- 343 18. Wolf, F. A. *et al.* PAGA: graph abstraction reconciles clustering with trajectory inference
344 through a topology preserving map of single cells. *Genome Biol.* **20**, 59–9 (2019).
- 345 19. Farrell, J. A. *et al.* Single-cell reconstruction of developmental trajectories during

- 346 zebrafish embryogenesis. *Science* **360**, eaar3131 (2018).
- 347 20. Edri, S., Hayward, P., Jawaid, W., Development, A. A. 2019. Neuro-mesodermal
348 progenitors (NMPs): a comparative study between pluripotent stem cells and embryo-
349 derived populations. *Development* doi:10.1242/dev.180190.supplemental
- 350 21. Gouti, M. *et al.* A Gene Regulatory Network Balances Neural and Mesoderm
351 Specification during Vertebrate Trunk Development. 1–27 (2017).
352 doi:10.1016/j.devcel.2017.04.002
- 353 22. Pankratz, M. T. *et al.* Directed Neural Differentiation of Human Embryonic Stem Cells via
354 an Obligated Primitive Anterior Stage. *Stem Cells* **25**, 1511–1520 (2007).
- 355 23. Thomson, M. *et al.* Pluripotency Factors in Embryonic Stem Cells Regulate Differentiation
356 into Germ Layers. *Cell* **145**, 875–889 (2011).
- 357 24. Jang, S. *et al.* Dynamics of embryonic stem cell differentiation inferred from single-cell
358 transcriptomics show a series of transitions through discrete cell states. *Elife* **6**, 91
359 (2017).
- 360 25. Alexander, J. M. *et al.* Brg1 modulates enhancer activation in mesoderm lineage
361 commitment. *Development* **142**, 1418–1430 (2015).
- 362 26. Takeuchi, J. K. *et al.* Chromatin remodelling complex dosage modulates transcription
363 factor function in heart development. *Nature Communications* **2**, 187–11 (2011).
- 364 27. Ho, L. *et al.* An embryonic stem cell chromatin remodeling complex, esBAF, is essential
365 for embryonic stem cell self-renewal and pluripotency. *Proc. Natl. Acad. Sci. U.S.A.* **106**,
366 5181–5186 (2009).
- 367 28. Kadam, S. & Emerson, B. M. Transcriptional specificity of human SWI/SNF BRG1 and
368 BRM chromatin remodeling complexes. *Molecular Cell* **11**, 377–389 (2003).
- 369 29. Raab, J. R., Runge, J. S., Spear, C. C. & Magnuson, T. Co-regulation of transcription by
370 BRG1 and BRM, two mutually exclusive SWI/SNF ATPase subunits. *Epigenetics*
371 *Chromatin* 1–15 (2017). doi:10.1186/s13072-017-0167-8
- 372 30. Corces, M. R. *et al.* An improved ATAC-seq protocol reduces background and enables
373 interrogation of frozen tissues. *Nat Meth* **14**, 959–962 (2017).
- 374 31. Wamstad, J. A. *et al.* Dynamic and coordinated epigenetic regulation of developmental
375 transitions in the cardiac lineage. *Cell* **151**, 206–220 (2012).
- 376 32. Rhee, H. S. *et al.* Expression of Terminal Effector Genes in Mammalian Neurons Is
377 Maintained by a Dynamic Relay of Transient Enhancers. *Neuron* **92**, 1252–1265 (2016).
- 378 33. Nora, E. P. *et al.* Targeted Degradation of CTCF Decouples Local Insulation of
379 Chromosome Domains from Genomic Compartmentalization. *Cell* **169**, 930–944.e22
380 (2017).
- 381 34. Alver, B. H. *et al.* The SWI/SNF chromatin remodelling complex is required for
382 maintenance of lineage specific enhancers. *Nature Communications* **8**, 14648 (2017).
- 383 35. Li, C. *et al.* Concerted genomic targeting of H3K27 demethylase REF6 and chromatin-
384 remodeling ATPase BRM in Arabidopsis. *Nat Genet* **48**, 687–693 (2016).
- 385 36. Tie, F., Banerjee, R., Conrad, P. A., Scacheri, P. C. & Harte, P. J. Histone Demethylase
386 UTX and Chromatin Remodeler BRM Bind Directly to CBP and Modulate Acetylation of
387 Histone H3 Lysine 27. *Molecular and Cellular Biology* **32**, 2323–2334 (2012).
- 388 37. Zhu, Q. *et al.* The transcription factor Pou3f1 promotes neural fate commitment via
389 activation of neural lineage genes and inhibition of external signaling pathways. *Elife* **3**,
390 2–21 (2014).
- 391 38. Kattman, S. J. *et al.* Stage-specific optimization of activin/nodal and BMP signaling
392 promotes cardiac differentiation of mouse and human pluripotent stem cell lines. *Cell*
393 *Stem Cell* **8**, 228–240 (2011).
- 394 39. Paulsen, M., Legewie, S., Eils, R., Karaulanov, E. & Niehrs, C. Negative feedback in the

- 395 bone morphogenetic protein 4 (BMP4) synexpression group governs its dynamic
396 signaling range and canalizes development. in **108**, 10202–10207 (National Academy of
397 Sciences, 2011).
- 398 40. Arias, A. M. & Hayward, P. Filtering transcriptional noise during development: concepts
399 and mechanisms. *Nat Rev Genet* **7**, 34–44 (2006).
- 400 41. Bier, E. & De Robertis, E. M. EMBRYO DEVELOPMENT. BMP gradients: A paradigm for
401 morphogen-mediated developmental patterning. *Science* **348**, aaa5838–aaa5838 (2015).
- 402 42. Eling, N., Richard, A. C., Richardson, S., Marioni, J. C. & Vallejos, C. A. Correcting the
403 Mean-Variance Dependency for Differential Variability Testing Using Single-Cell RNA
404 Sequencing Data. *Cell Systems* **7**, 284–294.e12 (2018).
- 405 43. Enver, T. & Teschendorff, A. E. Single-cell entropy for accurate estimation of
406 differentiation potency from a cell’s transcriptome. *Nature Communications* **8**, 1–
407 15 (2017).
- 408 44. Thompson, K. W., Marquez, S. B., Lu, L. & Reisman, D. Induction of functional Brm
409 protein from Brm knockout mice. *Oncoscience* **2**, 349–361 (2015).
- 410 45. Dupin, E., Calloni, G. W., Coelho-Aguiar, J. M. & Le Douarin, N. M. The issue of the
411 multipotency of the neural crest cells. *Developmental Biology* **444 Suppl 1**, S47–S59
412 (2018).
- 413 46. Motohashi, T. & Kunisada, T. Extended multipotency of neural crest cells and neural
414 crest-derived cells. *Curr. Top. Dev. Biol.* **111**, 69–95 (2015).
- 415 47. Srivastava, D. & DeWitt, N. In Vivo Cellular Reprogramming: The Next Generation. *Cell*
416 **166**, 1386–1396 (2016).
- 417 48. Tursun, B., Patel, T., Kratsios, P. & Hobert, O. Direct conversion of *C. elegans* germ cells
418 into specific neuron types. *Science* **331**, 304–308 (2011).
- 419 49. Cheloufi, S. *et al.* The histone chaperone CAF-1 safeguards somatic cell identity. *Nature*
420 **528**, 218–224 (2015).
- 421 50. Kolundzic, E. *et al.* FACT Sets a Barrier for Cell Fate Reprogramming in *Caenorhabditis*
422 *elegans* and Human Cells. *Developmental Cell* **46**, 611–626.e12 (2018).
- 423 51. Jiang, Z. *et al.* Knockdown of Brm and Baf170, Components of Chromatin Remodeling
424 Complex, Facilitates Reprogramming of Somatic Cells. *Stem Cells and Development* **24**,
425 2328–2336 (2015).
- 426 52. Lalit, P. A. *et al.* Lineage Reprogramming of Fibroblasts into Proliferative Induced Cardiac
427 Progenitor Cells by Defined Factors. *Cell Stem Cell* **18**, 354–367 (2016).
- 428 53. Singhal, N., Esch, D., Stehling, M. & Schöler, H. R. BRG1 Is Required to Maintain
429 Pluripotency of Murine Embryonic Stem Cells. *Biores Open Access* **3**, 1–8 (2014).
- 430 54. Takeuchi, J. K. & Bruneau, B. G. Directed transdifferentiation of mouse mesoderm to
431 heart tissue by defined factors. *Nature* **459**, 708–711 (2009).
- 432 55. Treutlein, B. *et al.* Dissecting direct reprogramming from fibroblast to neuron using single-
433 cell RNA-seq. *Nature* **534**, 391–395 (2016)

434
435
436

437

438

439

440 **Methods**

441 **Cell culture and in-vitro differentiations**

442 Mouse embryonic stem cells (ESCs) were cultured in media containing fetal bovine serum
443 (FBS) and leukemia inhibitory factor (LIF) without feeder mouse embryonic fibroblast cells with
444 daily media change at 37°C, 7% CO₂ and 85% relative humidity. CMs were differentiated as
445 described previously^{31,38}. Briefly, mouse ESCs were cultured in presence of ascorbic acid
446 (50µg/ml) in suspension cultures without LIF and Serum for 2 days to form embryoid bodies
447 (EBs). EBs were dissociated and treated for 2 days with VEGF, Activin A and BMP4 to induce
448 cardiac mesoderm which were subsequently dissociated and cultured as monolayer in presence
449 of FGF-basic (FGF2) and FGF10 for 6 days to form beating cardiac myocytes. *Brg1* was deleted
450 in presence of 200 nM 4-hydroxytamoxifen for 48 h with control cells treated similarly with
451 tetrahydrofuran^{5,25,56}. Neural stem cell differentiations were carried out in presence FGF2 and
452 epidermal growth factor (EGF), with growth factor removal forming neuronal progenitor cells as
453 described previously⁵⁷.

454

455 **Cell line and mouse line generation**

456 BRM was targeted using CRISPR/Cas9 with sgRNA targeting exon 2 following the described
457 protocol⁵⁸. sgRNA were cloned to a BbsI-digested pX330 vector (Addgene Cat #42230) by
458 annealing the following primers: 5' **caccg** GTCCACTGTGGATCCATGAA 3' and 5' **aaac**
459 TTCATGGATCCACAGTGGAC **c** 3' (bold indicates the BbsI digestion site). For construction of
460 BRM-3xFLAG tag line, we followed a similar strategy to insert 3xFLAG tag sequence between
461 the stop and penultimate codon using the following primers to clone sgRNA to the BbsI site of
462 pX330 vector : 5' caccg CTGATAACGAGTGACCATCC 3' and 5' aaac
463 GGATGGTCACTCGTTATCAG C 3'. The following sequence was inserted to the upstream

464 homology sequence for the insertion of 3x-FLAG tag: 5' ggaggcgggtggagcc GAC TAC AAG GAC
465 CAC GAC GGC GAC TAC AAG GAC CAC GAC ATC GAC TAC AAG GAC GAC GAC GAC
466 AAG TGA 3'. BRM targeting vectors were constructed by cloning 450 to 500 bp of DNA
467 upstream and downstream of midpoint of sgRNA target site into KpnI-XhoI and BamH1-NotI
468 sites of pFPF (a derivative of Addgene plasmid #22678 in which neomycin is replaced with
469 puromycin cassette). BRM-AID strain was constructed following a previously-described
470 strategy³³. Briefly, pEN244-CTCF-AID_71-114_-eGFP-FRT-Blast-FRT plasmid (addgene
471 Cat#92140) was digested with BamH1 and Sal1 and replaced the 3' and 5' homology of *Ctcf*
472 with that of *Brm* respectively. The following primers were used to clone an sgRNA to pX330
473 vector: 5' CAC CCT GAT AAC GAG TGA CCA TCC 3' and 5' GAC TAT TGC TCA CTG GTA
474 GGC AAA 3'. 2.5 µg of each of the sgRNA plasmid, plus 20 µg of *Brm* targeting constructs were
475 used for transfection. Single clones were selected, grown, PCR genotyped and DNA
476 sequenced.

477
478 For constructing a *Brm* mouse strain, we used CRISPR/Cas9 with the exact same exon 2
479 sgRNAs as in the cell line cloned to a BbsI-digested pX330 vector by annealing oligos: 5' **caccg**
480 **GTCCACTGTGGATCCATGAA** 3' & 5' **aaac** **TTCATGGATCCACAGTGGAC c** 3'. In-vitro
481 transcribed RNA and CAS9 protein complex and were injected to the embryos and transferred
482 to 0.5 dpc pseudo- pregnant female mice. We obtained a mouse line with 8bp deletion resulting
483 in a premature stop codon, confirmed by genotyping PCR sequencing and loss of BRM protein
484 by western blot

485

486 **siRNA mediated knockdown**

487 RNA knockdown were carried out using Lipofectamine-RNAiMax reagent (ThermoFisher,
488 13778150) and pre-designed siRNA against POU3F1 (Sigma, SASI_Mm02_00319981) and
489 REST (Sigma, SASI_Mm01_00196017) mRNAs. Control siRNA were used as negative controls
490 (Sigma, SIC001-10NMOL). Briefly, cells were split, washed and suspended in suspension culture
491 plates (for D0 differentiation) or monolayer (D4 differentiation). siRNAs (3 μ l of 10 μ M conc.) and
492 RNAiMax (7 μ l) were mixed separately with 75 μ l Optimem (Thermofisher, 31985062).
493 Knockdown was initiated by mixing both siRNA and RNAiMAX suspensions together, incubated
494 for 5 mins at RT. The entire 160 μ l of silencing mix were added dropwise to 1ml culture or
495 scaled accordingly.

496

497 **Nuclear extracts and Western blot**

498 Nuclear extracts were prepared using protocols described previously⁵⁹. Western blotting was
499 performed using standard techniques with PVDF membranes. Primary antibodies used were
500 anti- BRG1 (Abcam, ab110641, 1:1000), anti-FLAG (Sigma, F1804, 1:1000), anti-BAF170
501 (Bethyl, 1:1000, A301-39A), anti-BAF60c (Cell Signaling Technology, 62265, 1:1000), anti-
502 REST (EMD-Millipore, 07-579, 1:1000), anti-POU3F1 (Abcam, ab126746, 1:1000), or anti-TBP
503 (Abcam, ab51841, 1:2000), Vinculin (Sigma-Aldrich V9131, 1:1000), phospho-Smad (CST
504 9511, 1:1000) and , Smad1 (CST 9743, 1:1000). Secondary antibodies used were donkey anti-
505 rabbit IRDye 800cw (Licor, 926-32213, 1: 10,000), donkey anti-mouse IRDye 800cw (Licor, 925-
506 32212, 1: 10,000) and donkey anti-goat IRDye 680cw (Licor, 925-68074-1:10,000), HRP-linked-
507 anti-mouse (Cell Signaling Technology, 7076, 1:10000) or HRP-linked-anti-rabbit (Cell Signaling
508 Technology, 7074, 1:10000).

509

510 **Immunofluorescence**

511 Cells in monolayer were fixed for 30mins in 4% para-formaldehyde, permealized in 0.1% Triton
512 X and 5% goat serum in PBS for 1 hr and incubated with primary antibody (anti-FLAG (Sigma,
513 F1804, 1:300), anti-OCT4 (R&D, MAB1759, 1:300), anti-SOX2 (Abcam, ab97959, 1:300), anti-
514 NANOG (Abcam, ab80892, 1:300), anti-cardiac Troponin T (*Thermo Scientific, MS-295-P*,
515 1:100), or TUBB3 (BioLegend, 8012 1:5000) overnight. They were then washed thrice with 0.1%
516 triton X in PBS, incubated with secondary antibody (Goat anti-mouse Alexa 594 (Invitrogen,
517 A11005, 1:1000), Goat anti-rabbit Alexa594 (Invitrogen, 110037, 1:1000) or Donkey-anti-goat
518 AlexaFluor594, 1:1000) for 1hr at RT. Wells were washed thrice and stained with DAPI (1:1000
519 dilution) for 1-2 min followed by a PBS wash. Images were taken in Keyence confocal
520 microscope at 10x or Zeiss Spinning Disk microscope at 63x (for Extended Data Fig. 5a)
521 magnification.

522

523 **Flow cytometry**

524 At D10 of differentiation, WT and BRM KO cells were dissociated using TrypLE and fixed with
525 4% methanol-free formaldehyde. Cells were washed with PBS and permeabilized using
526 FACS buffer (0.5% w/v saponin, 4% Fetal Bovine Serum in PBS). For evaluation of
527 differentiation efficiency, cells were stained with a mouse monoclonal antibody for cardiac
528 isoform Ab-1 Troponin at 1:100 dilution (ThermoFisher Scientific #MS-295-P) or the isotype
529 control antibody (ThermoFisher Scientific #14-4714-82) for 1 hour at room temperature. After
530 washing with FACS buffer, cells were stained with goat anti-mouse IgG Alexa 594 secondary
531 antibody at 1:200 dilution (ThermoFisher Scientific #A-11005) for 1 hour at room temperature.
532 Cells were then washed with FACS buffer, stained with DAPI for 2 minutes, rinsed, and filtered
533 with a 40-micron mesh. At least 10,000 cells were analyzed using the BD FACS Ariall and
534 results were processed using FlowJo (BD Bioscience).

535

536 **Bulk RNA-seq**

537 Total RNA was isolated from biologically triplicate samples using miRNeasy micro kit with on-
538 column DNase I digestion (Qiagen). RNA-seq libraries were prepared using the Ovation RNA-
539 seq system v2 kit (NuGEN). Libraries from the SPIA amplified cDNA were made using the
540 Ultralow DR library kit (NuGEN). RNA-seq libraries were analyzed using Bioanalyzer, quantified
541 using KAPA QPCR and paired-end 100 bp reads were sequenced using a HiSeq 2500
542 instrument (Illumina). RNA reads were aligned with TopHat2⁶⁰, counts per gene calculated using
543 feature Counts⁶¹ and edgeR⁶² was used for the analysis of differential expression. K-means
544 clustering and pheatmap functions in R were used to cluster and generate heatmaps. GO
545 enrichment analysis were performed using GO Elite⁶³.

546

547 **Single cell RNA-seq**

548 Single-cell libraries were prepared using Single Cell 3' Library Kit v2 (10x Genomics) according
549 to the manufacturer's protocol. Briefly, about 10, 000 cells were suspended in 0.04% ultrapure
550 BSA-PBS (McLab, #UBSA-500) for GEM generation. GEMs were reverse transcribed, and
551 single stranded DNA were isolated and cleaned. Then cDNA was amplified twice, fragmented,
552 end-repaired, A-tailed and index adaptor ligated, with Ampure cleanup (Beckman Coulter) after
553 each step. Libraries were PCR amplified and cleaned with Ampure beads before shallow
554 sequencing in a NextSeq 500. Read depth normalized libraries were re-sequenced in a
555 NovaSeq sequencer (Illumina).

556

557 Sequencing reads were aligned using Cell Ranger 2.0.2 or 3.0 to the mm9 mouse reference
558 genome. cellranger *aggr* was used to generate an aggregated read normalized data matrix of

559 samples. The filtered gene matrix was subsequently used to create a Seurat object for QC and
560 tSNE or UMAP visualizations as described in [https://satijalab.org/seurat/](https://satijalab.org/seurat/tutorial) tutorial⁶⁴.

561

562 **Seurat analysis**

563 Seurat package v2.3.4 was used to analyze single cell RNA sequencing data. Cells were filtered
564 to remove dead cells and doublets. After log-normalization, sources of unwanted variation,
565 including differences in the number of UMI, number of genes, percentage of mitochondrial reads
566 and differences between G2M and S phase scores were regressed using the *ScaleData*
567 function. Clustering was performed using the top 30 principal components and visualized using
568 Uniform Manifold Approximation and Projection (UMAP)¹⁷.

569

570 Differential gene expression tests were run using the *FindMarkers* function with min.pct set to
571 0.1 and logfc.threshold set to 0.25. Selected differentially expressed genes with an adjusted p-
572 value less than 0.05 from the Wilcoxon Rank Sum test were then displayed using the Dotplot
573 function.

574

575 **Cell trajectories and pseudotime analysis**

576

577 Single Cell Analysis in Python (Scanpy), version 1.4.5, was used for finding highly variable
578 genes (HVGs), computing dimensionality reduction, regressing unwanted sources of variation,
579 and building developmental trajectory. Two thousand HVGs were selected within each
580 differentiation time separately and merged, to capture differentiation-specific genes⁶⁴ Variations
581 were regressed from HVGs that encode for ribosomal and mitochondrial proteins. HVGs were
582 then scaled to unit variance and zero mean. Next, the regressed two thousand HVGs were
583 decomposed to fifty principal components using the SciPy, version 1.41, ARPACK Singular

584 Value Decomposition (SVD) solver. A k-nearest neighbor graph was then constructed from a
585 local neighborhood size of ten, using thirty principal components (PCs), the euclidean distance
586 metric, and the connectivity estimation of the manifold set to Unified Manifold Approximation
587 Projection (UMAP) The louvain-graph based clustering algorithm was then run at a resolution of
588 1.0 on the k-nearest neighbor graph⁶⁵. A developmental trajectory was resolved by assessing
589 the connectivities of the louvain clusters from the k-nearest neighbor graph, using partition-
590 based graph abstraction (PAGA)¹⁸. Finally, the UMAP embedding was recomputed using the
591 PAGA initialization to visualize the developmental trajectory at single cell resolution.

592
593 Pseudotime analysis was performed using the URD package¹⁹ (version 1.0.2). A single
594 expression matrix with data from three timepoints and WT and *Brm*^{-/-} in low and high BMP4
595 conditions was processed in Seurat v2.3.4, as described above. The object was then down-
596 sampled to retain 5000 cells per sample in the low BMP4 dataset or 3000 cells per sample in
597 the combined low and high BMP4 dataset. The down-sampled object was converted to an URD
598 object using the *seuratToURD* function. Cell-to-cell transition probabilities were calculated by
599 setting the number of nearest neighbors (knn) to the square root of total cells in the object.
600 *POU5F1*⁺ clusters from day 4 were set as ‘root’ and all day 10 clusters were set as ‘tip’ cells. An
601 URD tree was constructed by simulating biased random walks from each tip cluster to root.

602

603 **Signaling Entropy Analysis**

604 Gene-barcode matrices from single-cell RNA-sequencing of day 4 and 6 differentiation samples
605 were first filtered and normalized using the Seurat package implemented in R. The
606 “LogNormalize” method with a default scaling factor of 10,000 was applied for normalization.
607 Differentiation potency was next estimated for each cell within the datasets using the SCENT
608 algorithm implemented in R, which integrates a cell’s transcriptomic profile with existing protein-

609 protein interaction (PPI) maps to quantify signaling entropy⁴³. Higher entropy is an indication of
610 greater developmental potency. A human PPI map compiled from Pathway Commons was used
611 as input for an adjacency matrix (<https://github.com/aet21/SCENT>). Mouse Ensembl IDs were
612 converted into their human homologues using the *AnnotationTools* Bioconductor package. The
613 resulting set of genes were then integrated with the human PPI network. The entropy value for
614 each cell was normalized to the largest eigenvalue (maximum possible entropy) of the adjacency
615 matrix. Distributions of normalized entropy values for each sample were then plotted for
616 comparison.

617

618 **Differential Variability Testing with BASiCS**

619 To assess changes in gene expression variability while accounting for artefactual technical noise
620 and the confounding relationship between variance and mean, single-cell RNA-seq datasets were
621 analyzed via the BASiCS framework as implemented in R⁴². This approach produces gene-
622 specific estimates of residual over-dispersion: a metric describing how greatly a gene's variability
623 departs from what is expected given its mean expression. Quality control and filtering of gene-
624 barcode matrices was performed using the *BASiCS_Filter* function with default parameters.
625 Posterior estimates of mean and residual over-dispersion for each gene were computed using a
626 Markov chain Monte Carlo (MCMC) simulation with 40,000 iterations, log-normal prior and
627 regression analysis.

628

629 **ATACseq**

630 Assay for transposase-accessible chromatin using sequencing (ATAC-seq) was performed as
631 described³⁰ in two to four biological replicates. Briefly, 50,000 cells (>95% viability) were lysed,
632 washed and tagmented for 45 mins and 3 h for CP and CM cells, respectively. DNA was purified
633 and amplified using universal Ad1 and barcoded reverse primers³⁰. Libraries were purified,

634 quantified and analyzed on a bioanalyzer and sequenced on a NEB NextSeq 550 sequencer
635 using Illumina NextSeq 500/550 High Output v2 kit (150 cycles). Sequencing image files were
636 de-multiplexed and fastq files generated. Reads (paired end 75 bp) were trimmed and aligned to
637 mouse genome mm9 assembly using Bowtie 2⁶⁶ with a minimum mapping quality score of 30.
638 Statistically enriched bins with a P-value threshold set to 1×10^6 were used to call peaks⁶⁷.
639 UCSC genome browser and IGV were used to view the browser tracks. Deeptools package in
640 Galaxy⁶⁸ (usegalaxy.org) was used to pool multiple replicates to generate 1x genome coverage
641 (average of multiple samples) browser tracks. GREAT⁶⁹ was used to generate gene lists near
642 ATACseq sites within 100Kb.

643

644 **ChIPseq**

645 Chromatin immunoprecipitations of histone modifications (H3K27ac and H3K27me3) were
646 performed as described⁷⁰ with modifications. Briefly, cells were crosslinked with 1%
647 formaldehyde, and quenched with 0.125 M glycine. Frozen pellets (1×10^7) were thawed,
648 washed, dounced and digested with MNase. Chromatin was sonicated at output 4 for 30s twice
649 with a 1 min pause between cycles then centrifuged at 10,000 g for 10 min at 4°C and stored at
650 -80°C. Chromatin was diluted to fivefold, pre-cleared for 2 h followed by immunoprecipitation
651 with primary antibodies for 12-16 hours at 4°C (H3K27ac, Active motif 39133; H3K27me3, CST
652 9733s). 5% of samples were used as input DNA. Antibody-bound protein- DNA complexes were
653 immunoprecipitated using 25 μ l of M-280 goat anti- rabbit IgG or anti-mouse IgG dyna beads for
654 2 h, washed a total of ten times with buffers [twice with IP wash buffer 1 containing 50 mM
655 Tris.Cl (pH 7.4), 150 mM NaCl, 1% NP-40, 0.25% sodium deoxycholate and 1 mM EDTA), five
656 times with IP wash buffer 2 containing 100 mM Tris.Cl (pH 9.0), 500 mM LiCl, 1% NP-40 and
657 1% sodium deoxcholate, and then thrice with IP wash buffer 2 along with 150 mM NaCl for

658 increasing stringency and eluted with 200 μ l of elution buffer [10 mM TrisCl (pH 7.5), 1 mM
659 EDTA and 1%SDS) at 65°C for 30 mins. Samples were reverse crosslinked, digested with
660 proteinase K and RNase A, and purified using AMPure XP beads (Beckman Coulter). To
661 prepare libraries for sequencing, DNA was end repaired, A-tailed, adapter ligated (Illumina
662 TrueSeq) and PCR amplified for 14 cycles. PCR-amplified libraries were size selected (200 –
663 500 bps)and ampure purified. The concentration and size of eluted libraries was measured
664 (Qubit and Bioanalyzer) before single-end 75bp sequencing using a NEBNextSeq sequencer.

665 Chromatin IP with anti-FLAG antibodies (Sigma, F1806) to probe for BRM binding sites were
666 performed similarly except following modifications. 1) Cells were double crosslinked with 2 mM
667 disuccinimidyl glutarate (DSG) and 1% formaldehyde. 2) MNase digestion conditions were
668 adjusted to have optimal chromatin digestion yielding fragments sizes of 400 to 1Kb. 3)
669 Chromatin binding to antibody and initial two washes contained either 0.05% (low SDS) or 0.2%
670 (high SDS) conditions. 4) Bound protein was competitively eluted with 0.1mg/ml FLAG peptides
671 (ELIM biopharma) and remaining material at 65°C. We observed better ChIP signal over noise
672 at high SDS samples eluted with the FLAG peptides.

673 Reads (single end 75 bp) were processed as in ATACseq analysis. The HOMER⁷¹ motif
674 enrichment package was used to enrich DNA motifs in both ATACseq and ChIP-binding sites.
675 HOMER calculates the q-value of known motifs to statistically confirm to Benjamini-Hochberg
676 multiple hypothesis testing corrections.

677 **ATAC-seq and ChIP-seq analysis**

678 The raw sequence data in fastq files were aligned to the mouse genome build mm9 using
679 bowtie2 aligner⁶⁶. Open chromatin regions and regions marked by H3K27Ac for each sample
680 were called using the narrowPeak output of the MACS2 peak caller⁷². Regions marked by

681 H3K27me3 were called using the BCP⁷² peak caller. A consensus set of peaks across
682 replicates (across samples for each of the ATAC-seq and the histone modification ChIPs) is
683 defined using the *-everything* followed by *-merge* options of the bedops program⁷³. A peak is
684 included in the consensus set of peaks (for the ATAC-seq data or the particular histone
685 modification ChIP-seq data) if it includes a peak called by the relevant peak caller for at least
686 one of the associated replicates. The number of reads mapping to each of the consensus
687 regions for each of replicates using the *subread featureCounts* program⁶¹. This creates a matrix
688 of raw counts - the number of rows equals the number of consensus regions and the number of
689 columns equals the number of samples. Regions that don't have at least 5 reads in at least 2 of
690 the samples are filtered out. The raw counts matrix is then normalized using edgeR
691 bioconductor^{62,73} R package. For each data set, a linear model is fit for the mean normalized
692 signal in each of the filtered consensus region. This model allows for the main effects of
693 genotype (BRM KO versus Wild type), differentiation time (D0, D4, D6 and D10), conditions
694 (normalBMP4 vs high BMP4) and the interaction between these two variables. The significance
695 of the regions associated with genotype, condition and/or differentiation time is estimated by
696 testing the combined null hypothesis that the main effects of genotype, differentiation time and
697 the interaction effect of between these two variables are all equal to zero. The heatmap of
698 significantly associated regions (FDR < 0.1) is done using the pheatmap package in R.

- 699
700 56. Ho, L. *et al.* An embryonic stem cell chromatin remodeling complex, esBAF, is an
701 essential component of the core pluripotency transcriptional network. *Proc. Natl. Acad.*
702 *Sci. U.S.A.* **106**, 5187–5191 (2009).
703 57. Conti, L. *et al.* Niche-Independent Symmetrical Self-Renewal of a Mammalian Tissue
704 Stem Cell. *PLoS Biol* **3**, e283–13 (2005).
705 58. Cong, L. *et al.* Multiplex genome engineering using CRISPR/Cas systems. *Science* **339**,
706 819–823 (2013).
707 59. Abmayr, S. M., Yao, T., Parmely, T. & Workman, J. L. Preparation of nuclear and
708 cytoplasmic extracts from mammalian cells. *Curr Protoc Pharmacol* **Chapter 12**,
709 Unit12.3–12.3.10 (2006).
710 60. Kim, D. *et al.* TopHat2: accurate alignment of transcriptomes in the presence of
711 insertions, deletions and gene fusions. *Genome Biol.* **14**, R36 (2013).

- 712 61. Liao, Y., Smyth, G. K. & Shi, W. featureCounts: an efficient general purpose program for
713 assigning sequence reads to genomic features. *Bioinformatics* **30**, 923–930 (2014).
714 62. Robinson, M. D., McCarthy, D. J. & Smyth, G. K. edgeR: a Bioconductor package for
715 differential expression analysis of digital gene expression data. *Bioinformatics* **26**, 139–
716 140 (2010).
717 63. Zambon, A. C. *et al.* GO-Elite: a flexible solution for pathway and ontology over-
718 representation. *Bioinformatics* **28**, 2209–2210 (2012).
719 64. Satija, R., Farrell, J. A., Gennert, D., Schier, A. F. & Regev, A. Spatial reconstruction of
720 single-cell gene expression data. *Nat. Biotechnol.* **33**, 495–502 (2015).
721 65. Lambiotte, R., Delvenne, J. C. & Barahona, M. Laplacian Dynamics and Multiscale
722 Modular Structure in Networks. *arXiv.org physics.soc-ph*, arXiv:0812.1770–90 (2008).
723 66. Langmead, B. & Salzberg, S. L. Fast gapped-read alignment with Bowtie 2. *Nat Meth* **9**,
724 357–359 (2012).
725 67. Thomas, R., Thomas, S., Holloway, A. K. & Pollard, K. S. Features that define the best
726 ChIP-seq peak calling algorithms. *Brief. Bioinformatics* **18**, 441–450 (2017).
727 68. Afgan, E. *et al.* The Galaxy platform for accessible, reproducible and collaborative
728 biomedical analyses: 2018 update. *Nucleic Acids Research* **46**, W537–W544 (2018).
729 69. McLean, C. Y. *et al.* GREAT improves functional interpretation of cis-regulatory regions.
730 *Nat. Biotechnol.* **28**, 495–501 (2010).
731 70. O’Geen, H., Echipare, L. & Farnham, P. J. Using ChIP-seq technology to generate high-
732 resolution profiles of histone modifications. *Methods Mol. Biol.* **791**, 265–286 (2011).
733 71. Heinz, S. *et al.* Simple combinations of lineage-determining transcription factors prime
734 cis-regulatory elements required for macrophage and B cell identities. *Molecular Cell* **38**,
735 576–589 (2010).
736 72. Xing, H., Mo, Y., Liao, W. & Zhang, M. Q. Genome-Wide Localization of Protein-DNA
737 Binding and Histone Modification by a Bayesian Change-Point Method with ChIP-seq
738 Data. *PLoS Comput Biol* **8**, e1002613–12 (2012).
739 73. McCarthy, D. J., Chen, Y. & Smyth, G. K. Differential expression analysis of multifactor
740 RNA-Seq experiments with respect to biological variation. *Nucleic Acids Research* **40**,
741 4288–4297 (2012).
742

743 **Data availability**

744 Bulk and single cell RNAseq, ATACseq, and ChIPseq datasets have been deposited in GEO
745 under accession number GSE150186.

746

747 **Code availability**

748 Codes used to analyze single cell data on Seurat, generate heat maps, UMAPs and URD
749 figures will be available upon request.

750

751 **Author Contribution**

752 Project design and direction: B.G.B. and S.K.H. ES cell engineering, in vitro differentiation, gene
753 expression, scRNAseq, ATACseq, ChIPseq and data analysis: S.K.H. Additional scRNA-seq
754 analysis: A.P.B, K.R., under direction of B.G.B and I.S.K. Cell culture: A.M.B., K.S. Data
755 analysis: R.V.D. under direction of L.S.W. Manuscript writing: S.K.H and B.G.B with contribution
756 from all authors.

757

758 **Acknowledgements**

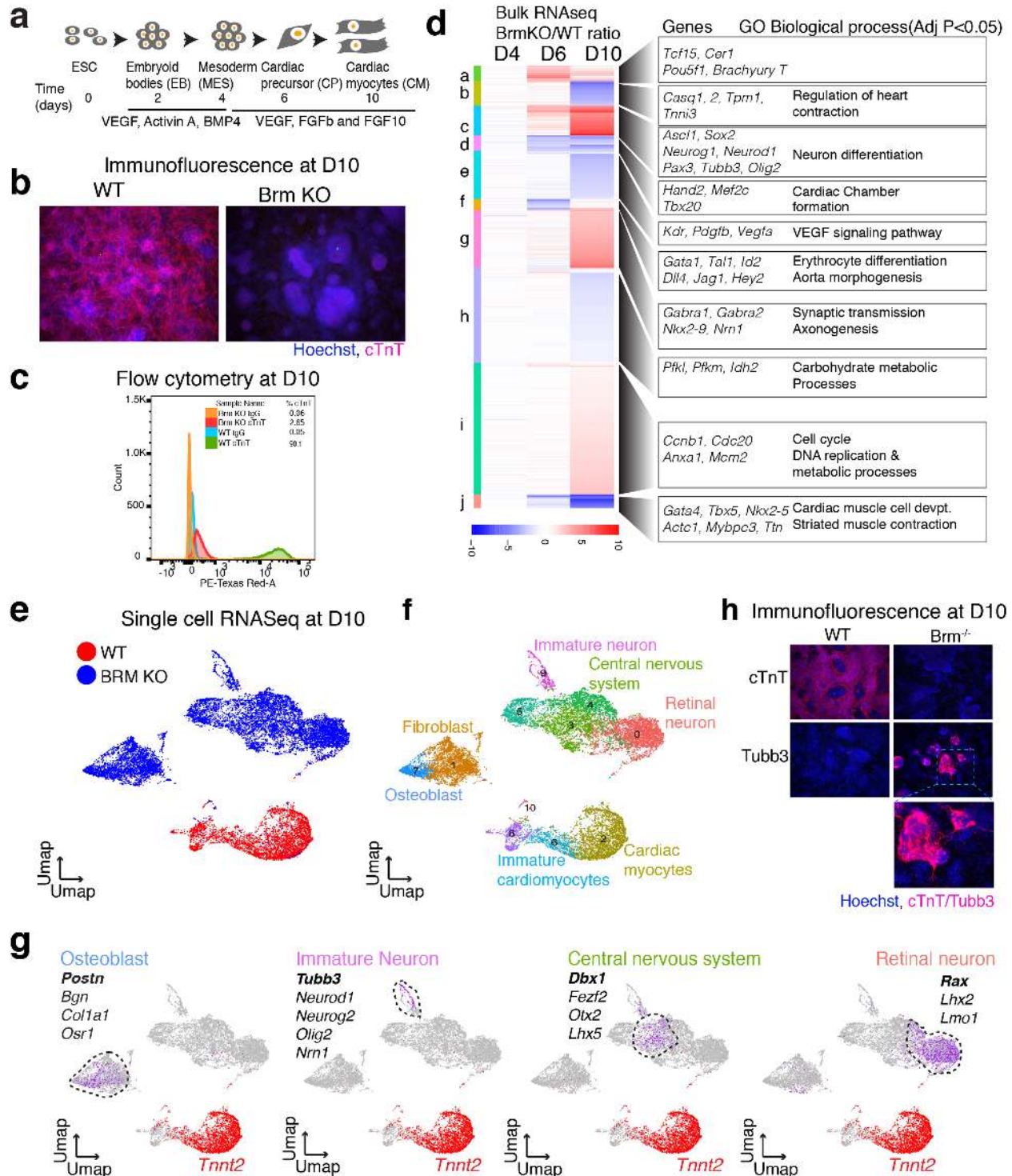
759 We thank Natasha Carli, Y. Hao, M. Bernardi, and J. McGuire (Gladstone Genomics Core) for
760 RNA-Seq and 10X Genomics library preparation, the UCSF Center for Applied Technologies for
761 sequencing, Elphege Nora for help with *Brm-AID* strain construction, Vasumathi Kameswaran
762 for help with BRM ChIP-seq, Reuben Thomas for ATAC-seq and ChIP-seq data analysis, J.
763 Zhang (Gladstone Transgenic Core) for knockout mouse production, and K. Claiborn for
764 editorial assistance. This work was supported by grants from the NIH/NHLBI (P01HL089707,
765 Bench to Bassinet Program UM1HL098179, and R01HL114948), to B.G.B; and postdoctoral
766 fellowships from the American Heart Association (13POST17290043), Tobacco Related
767 Disease Research Program (22FT-0079) and NIH training grant (2T32- HL007731 26) to S.K.H.
768 I.S.K. was supported by funds from the Society for Pediatric Anesthesia, Hellman Family Fund,
769 UCSF REAC Award and the UCSF Department of Anesthesia and Perioperative Care. This
770 work was also supported by an NIH/NCRR grant (C06 RR018928) to the J. David Gladstone
771 Institutes and by The Younger Family Fund (B.G.B.).

772

773 **Competing interests:** B.G.B. is a co-founder of Tenaya Therapeutics. The work presented here
774 is not related to the interests of Tenaya Therapeutics

775

776



777

778

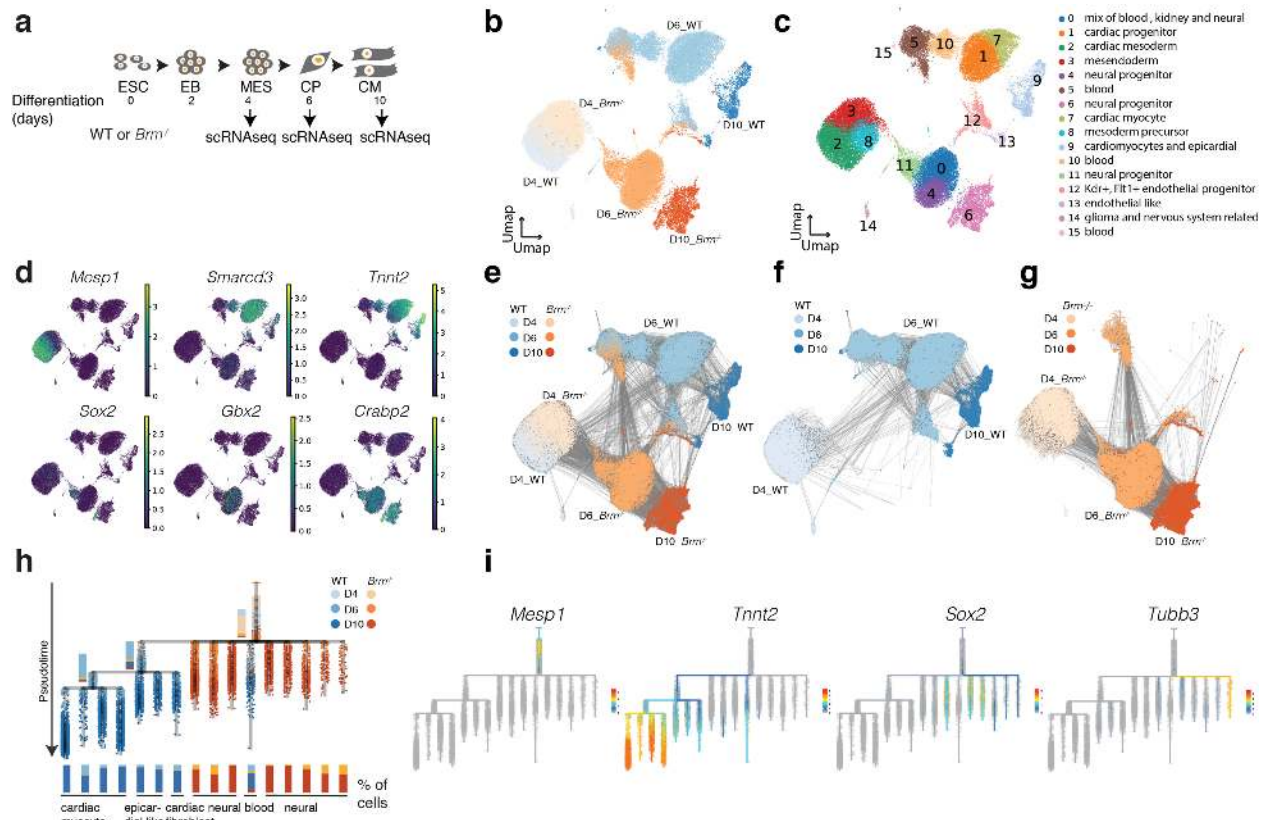
Fig. 1. BRM activates cardiac gene expression programs and represses neural genes

779

during directed cardiomyocyte differentiation

780 Cardiac differentiation scheme (**a**), estimation of cardiac myocyte at D10 of differentiation by
781 immunofluorescence (**b**) and flow cytometry (**c**) of cardiac Troponin T. **d**, Bulk RNAseq analysis
782 of WT and BRM KO cells at mesoderm (D4), cardiac precursor (D6) and cardiomyocyte (D10)
783 stages of differentiation. Counts per million (CPM) average of three replicates were plotted as a
784 ratio of WT over KO. Gene Ontology (GO) biological process enrichment were determined by
785 GOElite. Single cell RNAseq gene expression projected on a UMAP space for WT and BRM KO
786 at D10 (**e**), marker genes highlighted (**f**) and cell types inferred (**g**). **h**, immunofluorescence of
787 cardiac Troponin T and pan-neural progenitor marker TUBB3 (TUJ1) at D10 of cardiac
788 differentiation.

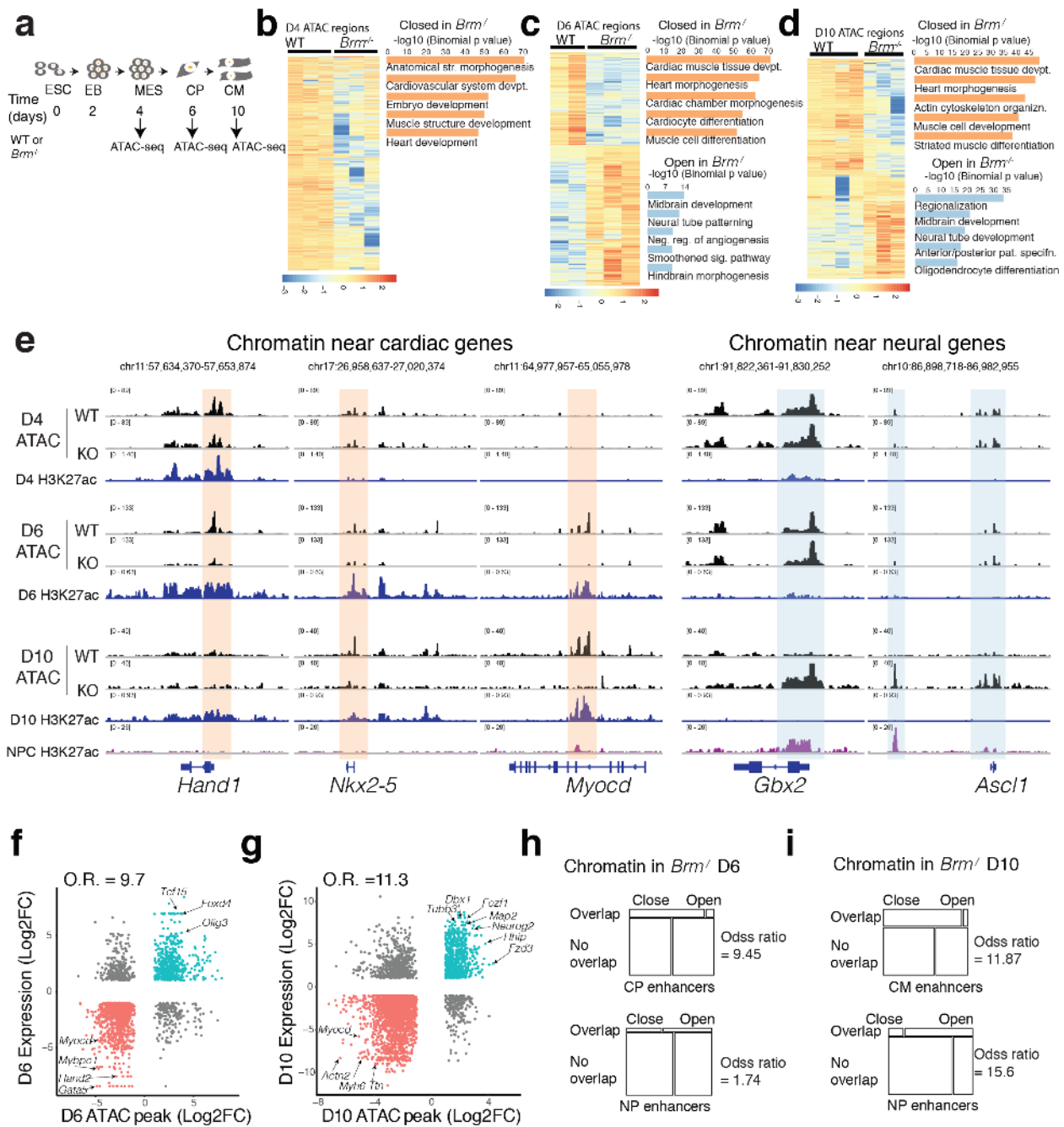
789
790
791
792
793
794
795
796



797
 798 **Fig. 2. Loss of BRM leads to acquisition of neural fate after pre-cardiac mesoderm**
 799 **formation**
 800 **a**, Scheme of cardiac differentiation and time of scRNAseq. **b-d**, Processed scRNAseq data
 801 projected on a UMAP space showing genotypes and days of differentiation (**b**), clusters with
 802 inferred cell types (**c**), and gene expression feature plots displaying expression of cardiac and
 803 neural genes along differentiation (**d**). **e-g**, Partition-based graph abstraction (PAGA) showing
 804 connectivity of cells for both WT and BRM KO together at D4, D6 and D10 of differentiation (**e**)
 805 and separately for WT (**f**) and BRM KO cells (**g**). **h-i**, Transcriptional trajectory analysis from
 806 single cell data showing step wise transition of WT cell from D4 to D10, and sudden acquisition
 807 of neural fate in BRM KO cells (**h**), with cardiac and neural marker expression shown along
 808 differentiation trajectory (**i**).

809
 810
 811

812



813

814

815

Fig. 3. BRM remodels enhancer chromatin to open cardiac and close non-cardiac

816 regulatory regions

817 a, Schematics of cardiac differentiation and timing of ATAC-seq. b-d, Heat map of significantly

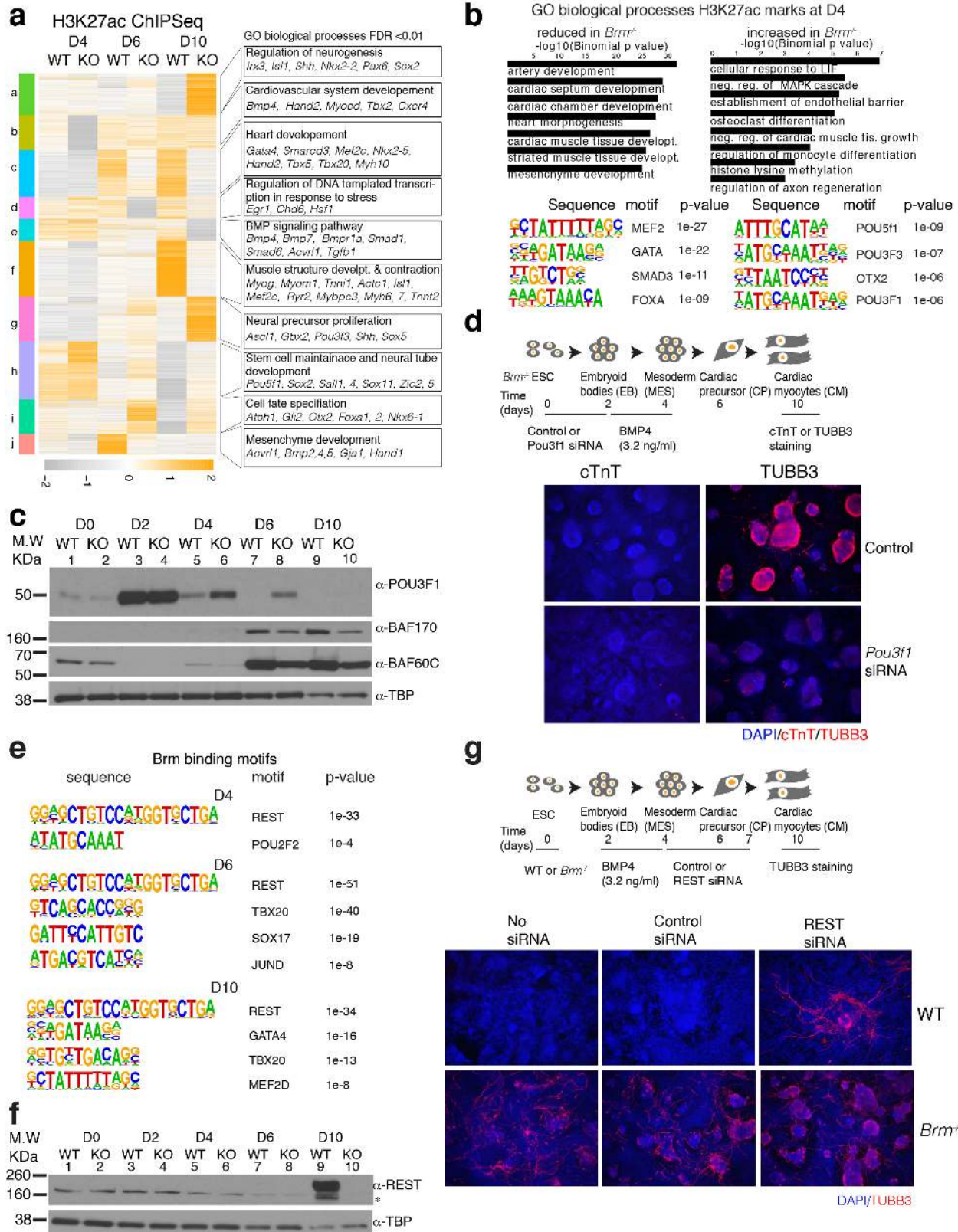
818 altered ATAC-seq peaks in WT and BRM KO at D4 (b), D6 (c) and D10 (d). GREAT enrichment

819 (two nearest genes within 100Kb) of gene ontology (GO) biological processes shown on the

820 right. **e**, Example browser tracks show ATAC-seq regions over promoter and regulatory regions
821 of key cardiac and neural genes along with D4, D6, D10 and neural progenitor cell enhancer
822 H3K27ac tracks. **f-g**, ATAC-seq peak strengths are correlated with the neighboring BRM
823 regulated genes (within 100Kb, FDR<0.05, ± 2 fold) at D6 (**f**) and D10 (**g**). **h-i**, BRM-mediated
824 open and close chromatin regions compared with cardiac and neural progenitor enhancers.
825 Closed and open chromatin in *Brm*^{-/-} at D6 (**h**) and at D10(**i**) are compared with respective
826 cardiac and neural progenitor enhancers.

827

828



829

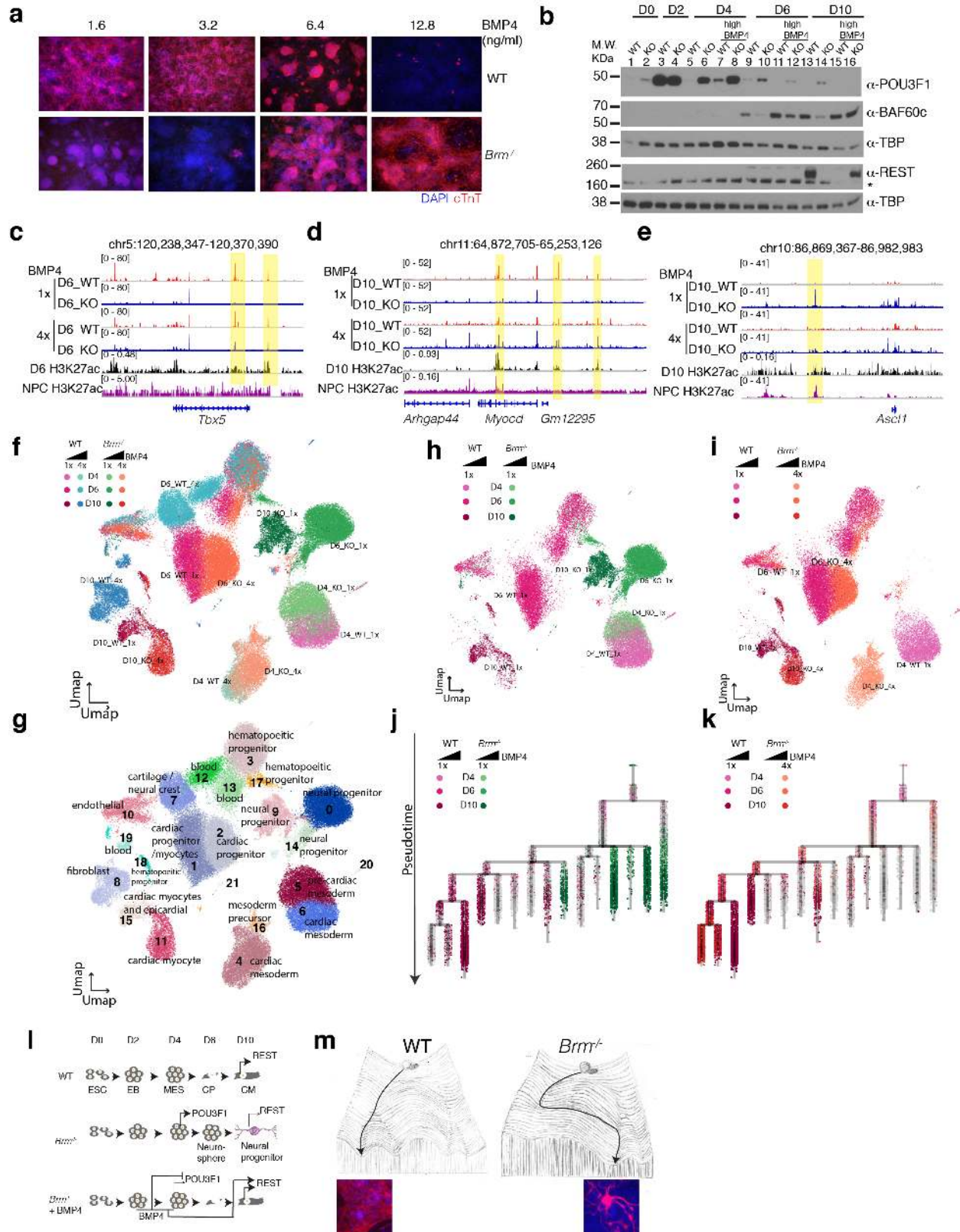
830

Fig. 4. BRM modulates expression of POU3F1 and REST to repress neurogenesis and

831

facilitate cardiogenesis.

832 **a**, Heat map of significantly affected (FDR<0.05, fold change 2) H3K27ac peaks due to loss of
833 BRM at D4, D6 and D10 of differentiation. GREAT analysis of GO biological processes enriched
834 (within 1mb) are shown to the right of the clusters. **b**, Biological process enriched at D4 for sites
835 that reduced (left) or gained (right) H3K27ac in absence of BRM. Corresponding motifs enriched
836 are shown underneath. **c**, Western blot of indicated proteins in WT and BRM KO cells during
837 cardiac differentiation. **d**, Scheme of *Pou3f1* knockdown during cardiac differentiation followed
838 by immunostaining with cTnT and TUBB3 at D10. **e**, Motifs enriched on BRM binding sites from
839 BRM3xFLAG ChIP-seq peaks at D4, D6 and D10. **f**, Western blot showing loss of REST
840 expression in BRM KO cells. **g**, Scheme of REST knockdown during cardiac differentiation
841 followed by TUBB3 immunostaining at D10.
842

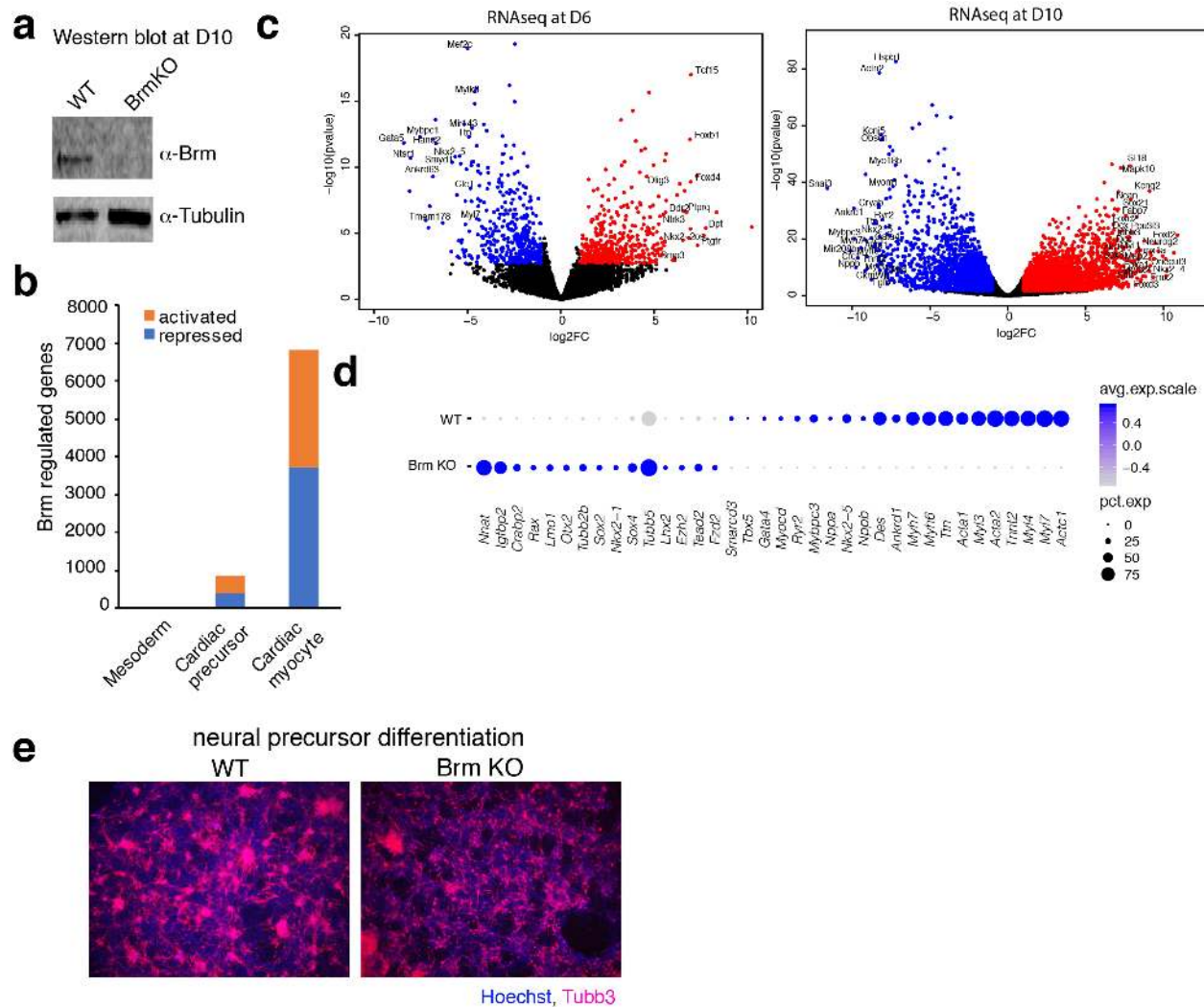


843
844

Fig. 5. BMP4 signaling rescues loss of BRM phenotype

845 **a**, Immunostaining of WT and BRM KO cells in presence of increasing concentrations of
846 exogenous BMP4. BMP4 treatment occurred at D2 to D4 of differentiation. **b**, Western blot
847 showing repression of POU3f1 and re-expression of REST and BAF60c in presence of high
848 BMP4 in BRM KO cells. **c-e**, Browser tracks showing re-opening of closed enhancer regions in
849 BRM KO cells in presence of high BMP4 at *Tbx5* (**c**) and *Myocd* (**d**) and closing of open
850 chromatin at *Ascl1* (**e**) loci at the yellow highlighted regions. **f-g**, Single cell RNAseq data
851 projected on a UMAP space showing both WT and BRM KO genotypes (**f**), clusters with inferred
852 cell types (**g**) at D4, D6 and D10 of differentiation induced with normal (1x, 3.2 ng/ml) and high
853 (4x, 12.8ng/ml) BMP4 concentrations. **h-i**, Both WT and BRM KO at normal BMP4
854 concentration show divergence in clustering in the UMAP space (**h**), while WT at normal BMP4
855 shows similar clustering with BRM KO at high BMP4 concentrations and occupy the same
856 UMAP space (**i**). **j-k**, Transcriptional trajectory analysis showing divergence in differentiation
857 path for WT and BRM KO cells at normal BMP4 concentrations (**j**), while WT at normal and
858 BRM KO at high BMP4 concentration make step-wise transition to form cardiomyocytes (**k**). **l**,
859 Model showing at normal BMP4 concentration, WT cells form cardiomyocytes and express
860 neuronal inhibitor REST. In *Brm*^{-/-} cells, neurogenic factor POU3F1 fails to be repressed
861 whereas REST is repressed, resulting in neural progenitor formation. *Brm*^{-/-} cells induced with
862 high BMP4 repress POU3F1 and re-express REST, forming cardiac myocytes. **m**, Waddington
863 landscape depicting WT differentiation forming cardiomyocytes, while *Brm*^{-/-} cells continue on a
864 cardiac differentiation path before undertaking a saddle-node bifurcation to form neural
865 progenitor cells.

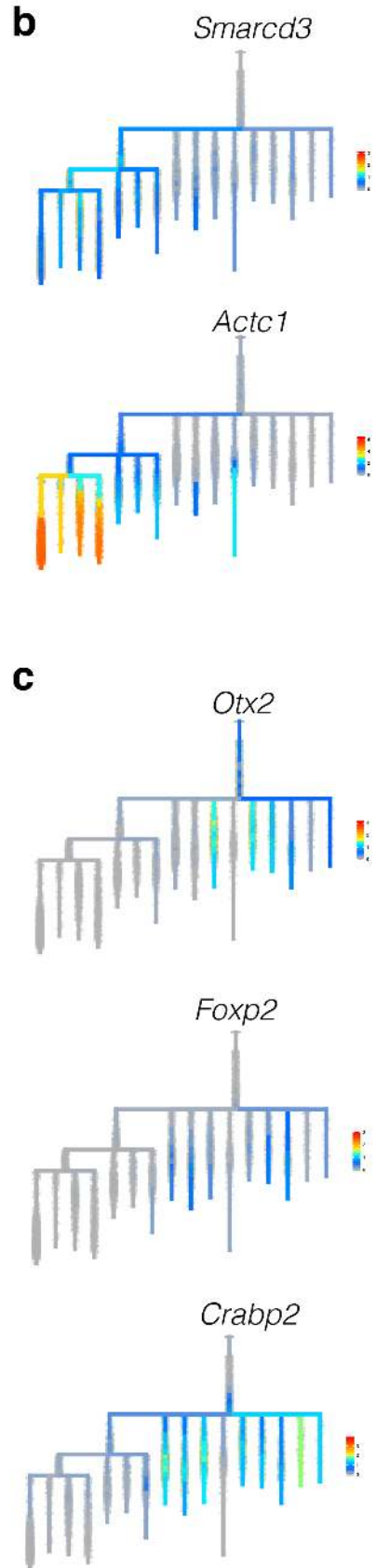
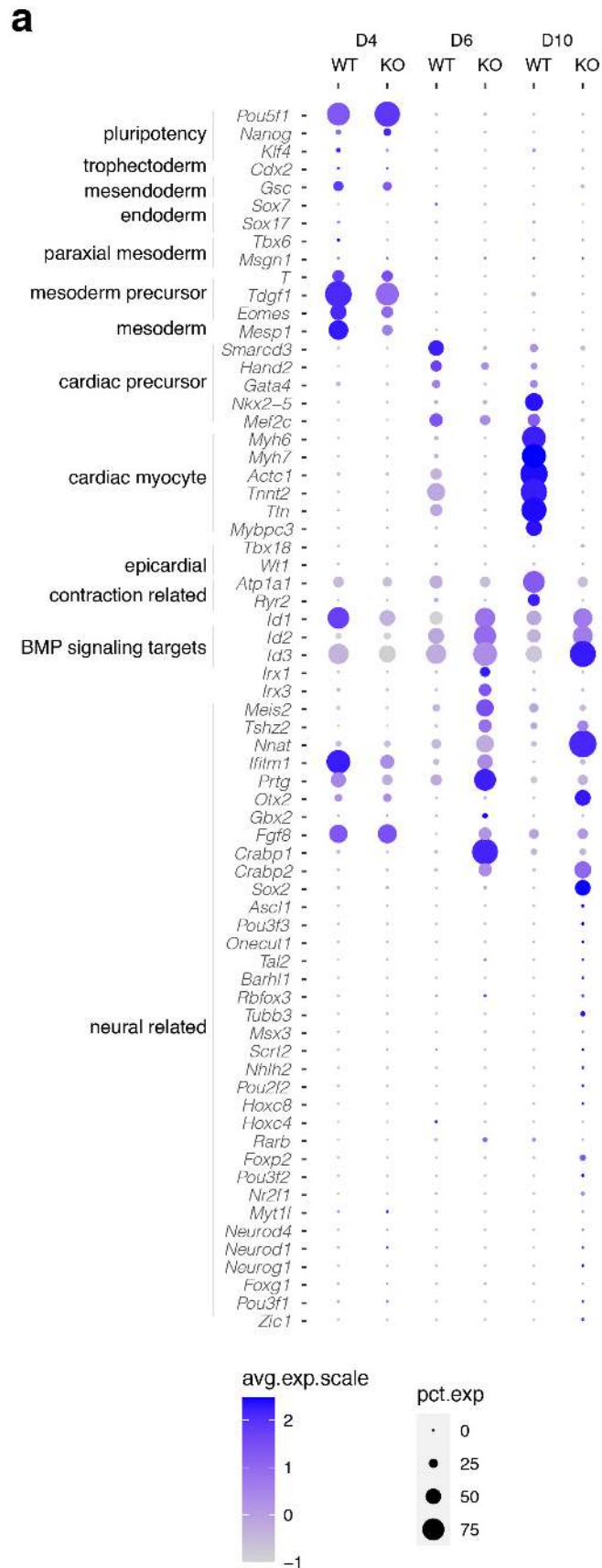
866



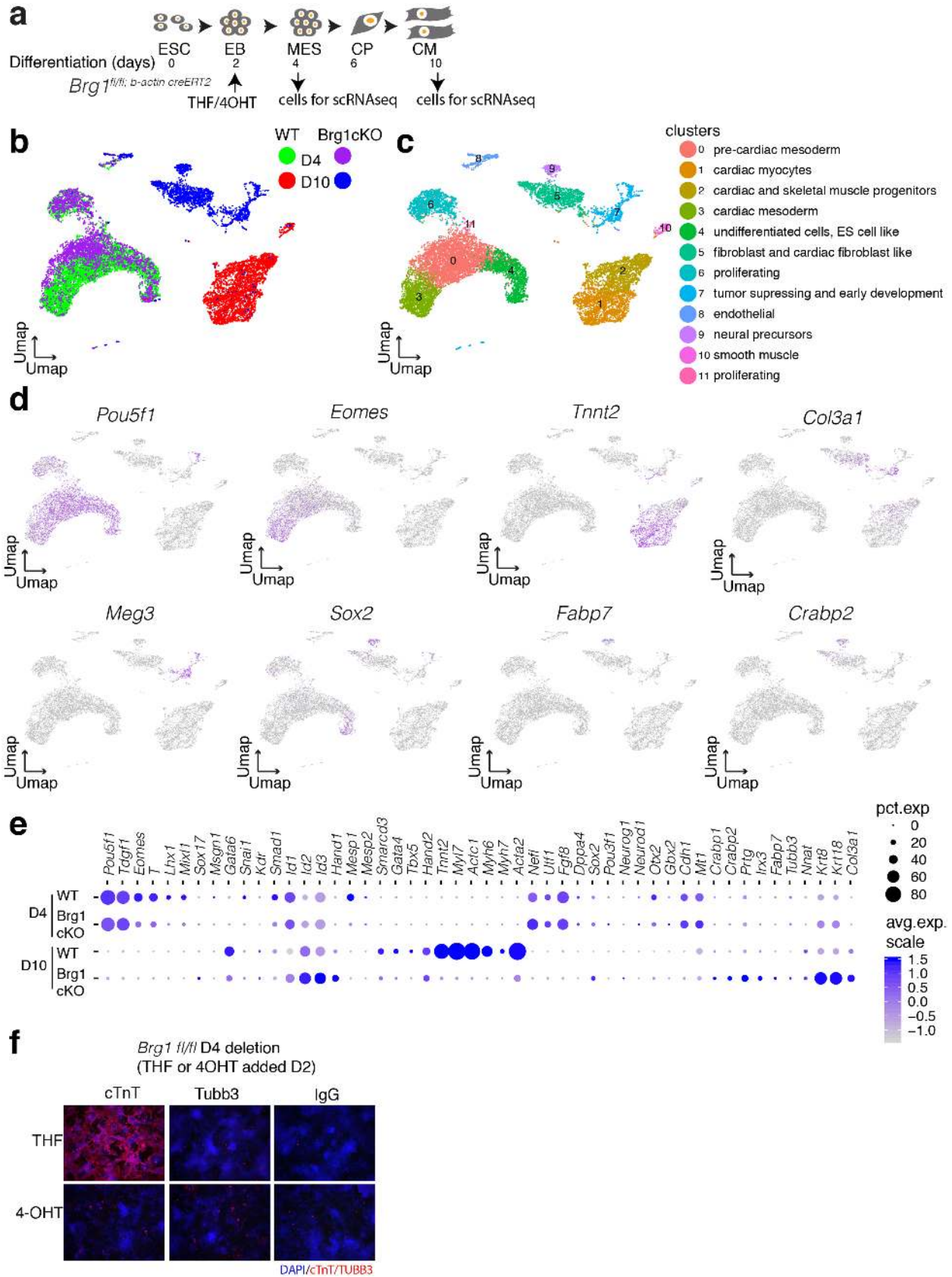
867
868

869 Extended Data Fig. 1. Loss of BRM leads to expression of neural genes in cardiac
870 differentiation and has minimal effect in neural differentiation

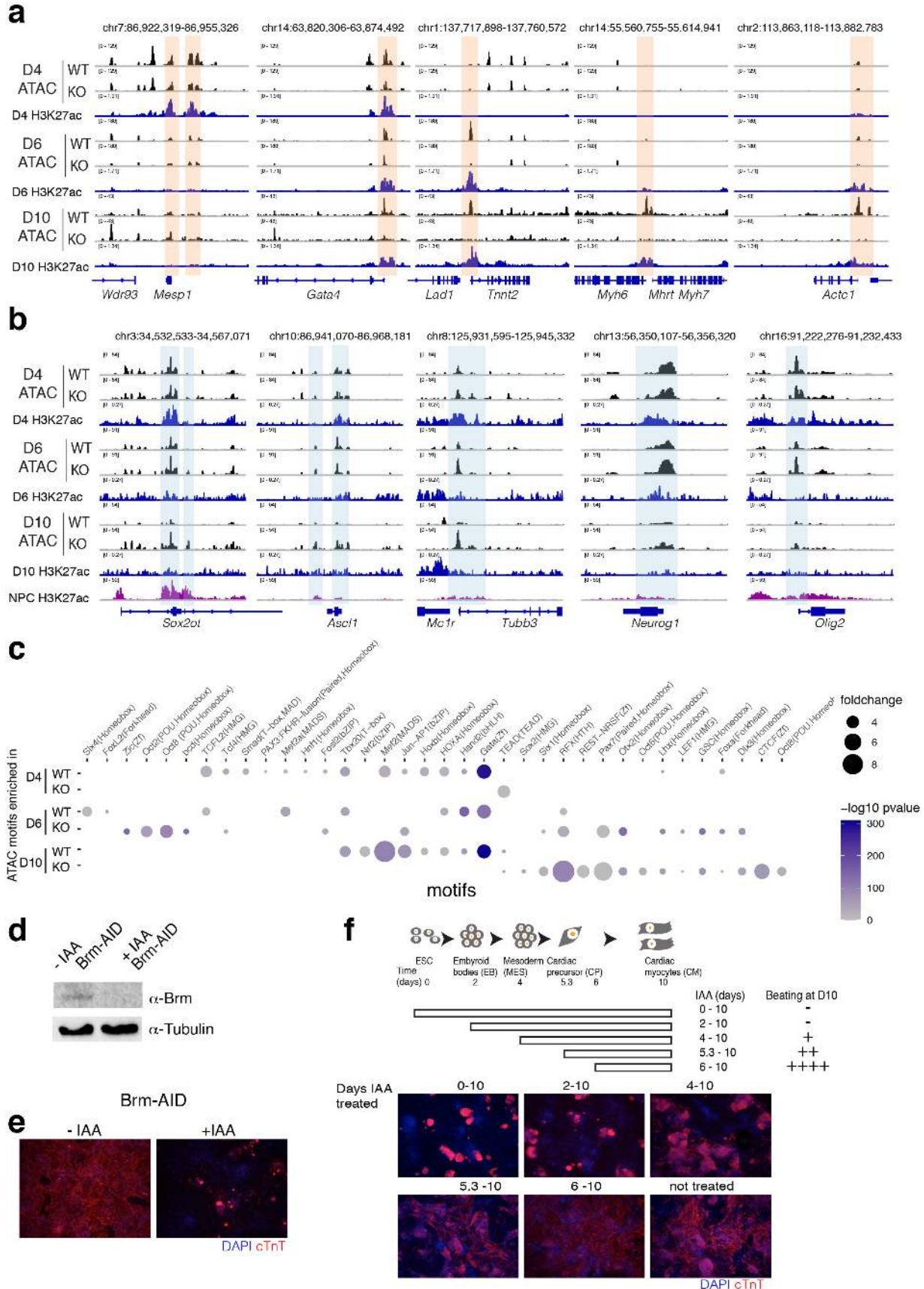
871 **a**, Western blot at D10 of cardiac differentiation of WT and BRM KO cells. **b**, Volcano plots of
872 RNA-seq data showing significantly (FDR<0.05 and fold change > 2) downregulated (blue) and
873 upregulated (red) genes at D6 and D10 stages of differentiation. **c**, Quantification of significantly
874 (FDR<0.05 and fold change > 2) de-regulated genes at D4 (mesoderm), D6 (cardiac precursor)
875 and D10 (cardiomyocyte) stages of differentiation. **d**, Dots plots showing expression of indicated
876 genes from D10 WT and BRM KO single cell RNA-seq data. **e**, TUBB3 immunostaining of WT
877 and BRM KO cells differentiated to neural precursor cells.



879 Extended Data Fig. 2. **Brm loss leads to expression of neural genes after D4 of**
880 **differentiation**
881 **a**, Dot plots showing quantitative bulk changes in gene expression between WT and BRM KO
882 cells at D4, D6 and D10 stages of differentiation for early developmental, cardiac mesoderm,
883 precursors, myocytes and genes enriched in BRM KO cells and a select set of genes involved in
884 neuroectoderm development. **b-c**, Feature plots of developmental trajectory analysis using URD
885 for selected cardiac (**b**) and neural genes (**c**)
886



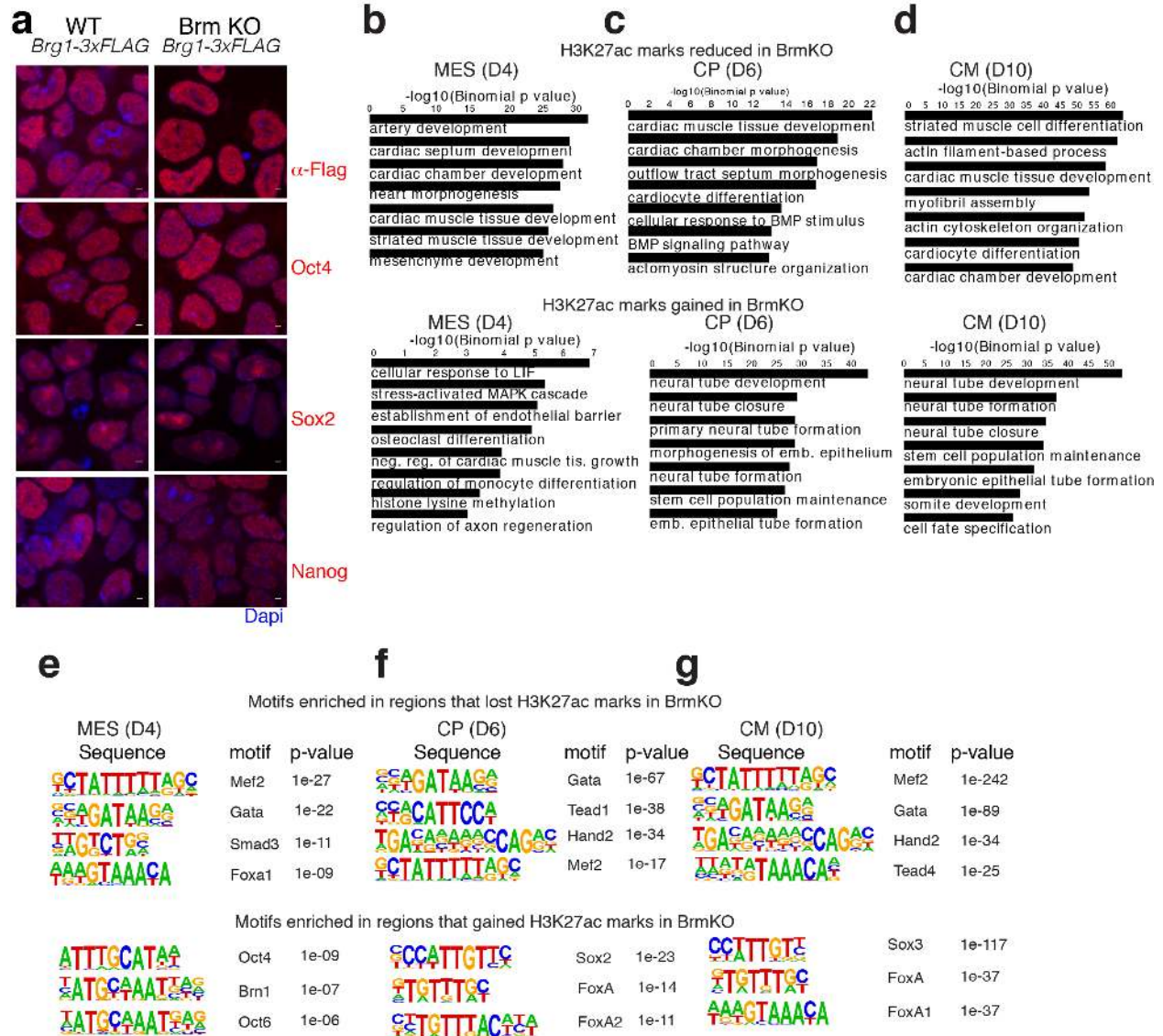
888 Extended Data Fig. 3. **Loss of BRG1 early in differentiation leads to formation of non-**
889 **cardiac cell types**
890 **a**, Scheme of cardiac differentiation showing timing of induction with 4-hydroxy tamoxifen or the
891 control tetrahydrofuran and scRNA-seq. **b-d**, UMAPs of single cell RNA-seq data at D4 and D10
892 of differentiation of WT and conditional BRG1 KO genotypes (**b**), clusters with inferred cell types
893 (**c**) and feature plots of expression of indicated genes (**d**). Dot plots comparing gene expression
894 quantification of WT and conditional BRG1 KO at D4 and D10 of differentiation. **e**, Cardiac
895 troponin T and TUBB3 immunostaining at D10 for WT and BRG1 cKO cells deleted at D2 of
896 differentiation. **f**, Immunostaining with cTnT at D10 with increasing concentration of BMP4.
897



899 Extended Data Fig. 4. **BRM is required during cardiac mesoderm formation**

900 **a-b**, ATAC-seq browser tracks showing WT and BRM KO chromatin accessibility at D4, D6 and
901 D10 of cardiac differentiation along with H3K27ac active enhancer marks at each of these
902 stages for a set of cardiac gene loci (**a**) and neural gene loci, along with neural precursor
903 H3K27ac marks (**b**). **c**, Motifs enriched at the open chromatin regions in WT and BRM KO cells
904 at D4, D6, D10 differentiation stages. **d-f**, Auxin inducible degron mouse ES strain of BRM
905 (Brm-AID) with or without auxin analog indole acetic acid (IAA) present throughout cardiac
906 differentiation shows BRM degradation by western blot (**d**), loss of cardiac myocyte by cTnT
907 immunostaining (**e**) and determines D0 to D4 as the window of BRM activity (**f**).

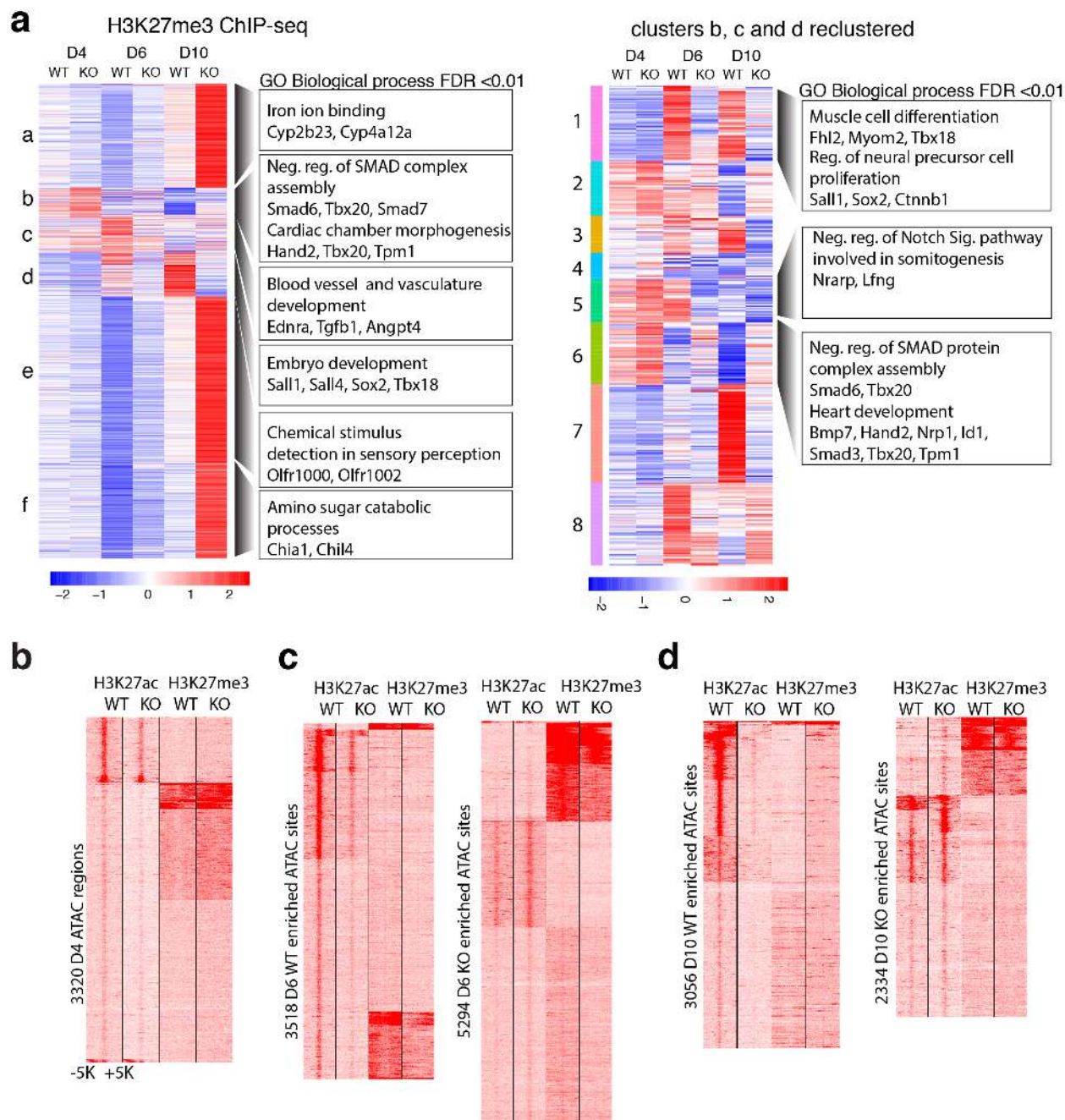
908



909
910 Extended Data Fig. 5. **BRM loss leads to reduced H3K27ac marks near cardiac and**
911 **increased H3K27ac marks near neural genes**

912 **a**, Immunostaining of WT and BRM KO ES cells with indicated pluripotency markers. Scale bars
913 are 2 μ m, magnification 63x. **b-d**, GO biological processes enriched for genes (within 1mb) near
914 sites that reduced (upper panels) or gained (lower panels) H3K27ac marks in BRM KO cells at
915 D4 (**b**), D6 (**c**) and D10 (**d**) of differentiation. **e-g**, Motifs enriched at the differentially enriched
916 sites in BRM KO cells are shown at D4 (**e**), D6 (**f**) and D10 (**g**) stages of cardiac differentiation
917 respectively.

918



919

920

921 Extended Data Fig. 6. **H3K27me3 marks are altered in BRM KO cells at D6 and D10 of**

922 **differentiation**

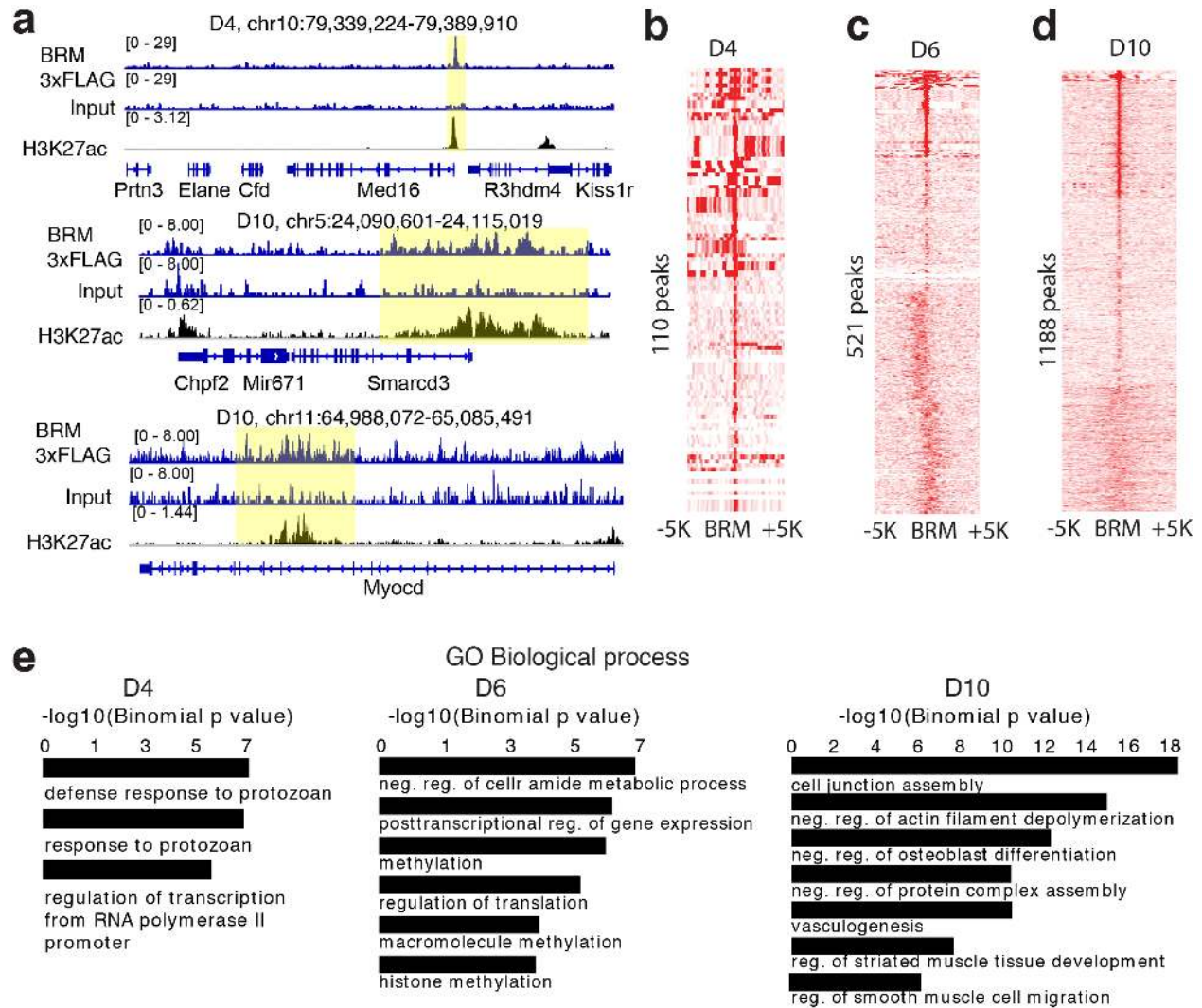
923 **a**, Differential enrichment of H3K27me3 marks in WT and BRM KO cells during cardiac

924 differentiation displayed in the form of a heat map. Cluster b, c, and d were re-clustered and

925 shown in a separate heat map (right) GREAT analysis of significant (Benjamini-Hochberg

926 adjusted p-value (FDR) <0.01) GO biological processes (within 1Mb) enrichment for the clusters
927 are on the right with representative genes shown. **b-d**, Correlation of ATAC-seq peaks to active
928 enhancer (H3K27ac) and Polycomb mediated repression (H3K27me3) at D4 (**b**), D6 (**c**) and
929 D10 (**d**) of differentiation.

930
931
932
933
934
935
936
937
938
939
940
941

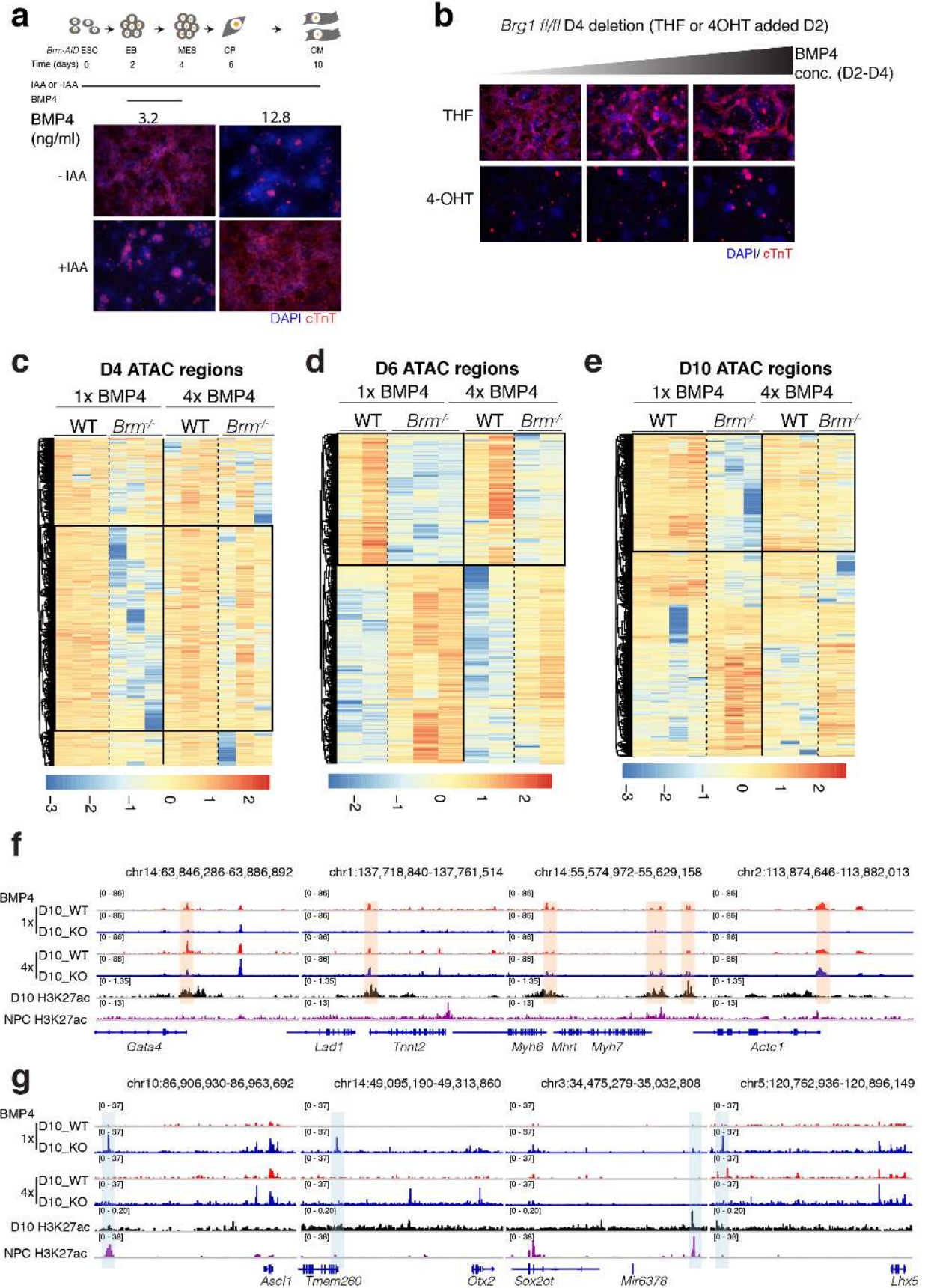


942
943

944 Extended Data Fig. 7. **ChIP-seq reveals increased BRM binding during cardiac**
945 **differentiation**

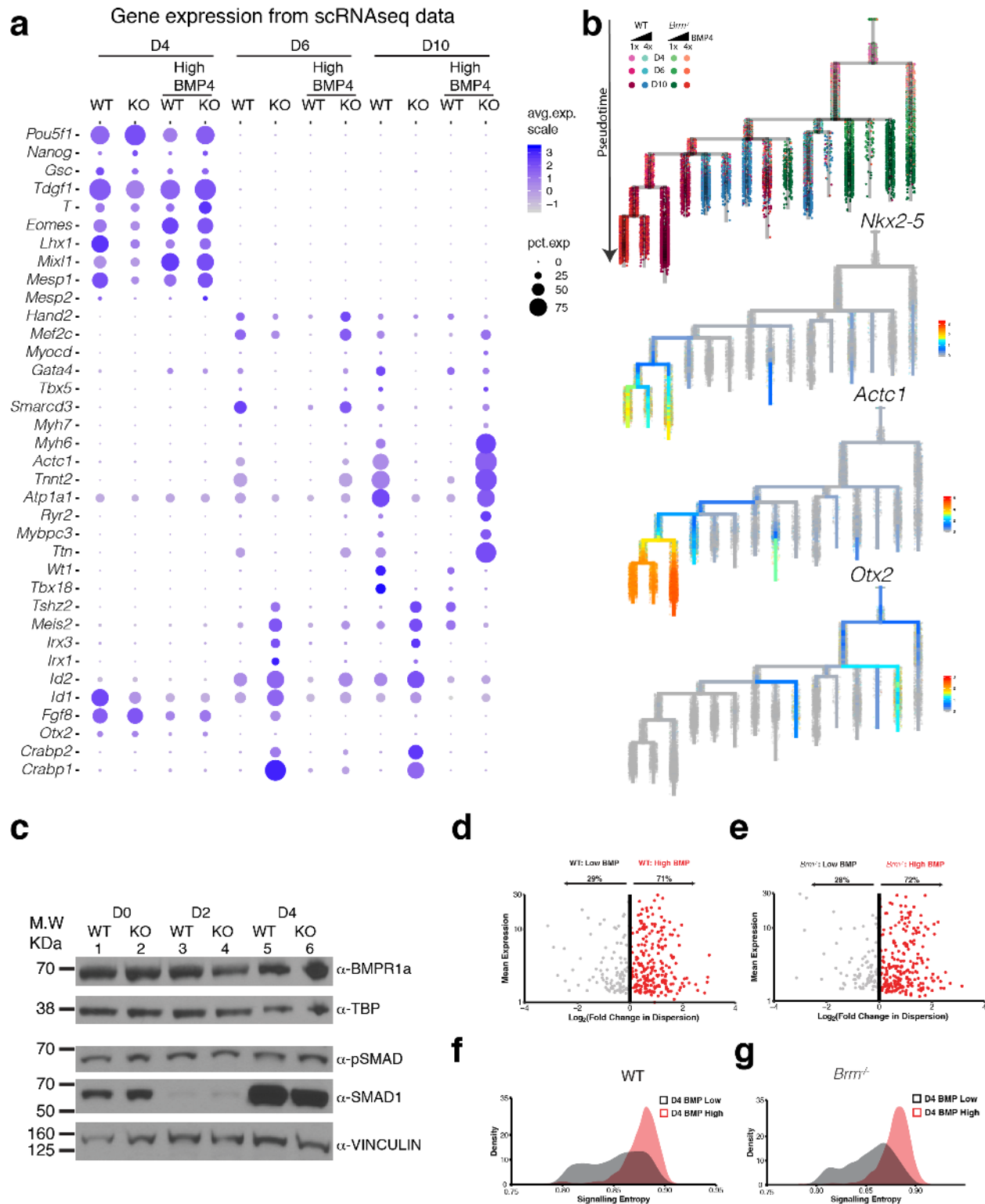
946 **a-d**, Genome browser (IGV) tracks showing BRM-3xFLAG ChIP-seq, corresponding input
947 samples and activating enhancer mark H3K27ac (**a**) and heat maps of BRM-3xFLAG ChIP-seq
948 over identified BRM binding sites at D4 (**b**), D6 (**c**) and D10 (**d**) of differentiation
949 biological processes enriched for BRM binding site (within 100kb) at the indicated differentiation
950 stages.

951
952



954 Extended Data Fig. 8. **BMP4 restores WT-like chromatin in *Brm*^{-/-} cells**

955 **a**, Scheme of cardiac differentiation showing timing of IAA and BMP4 addition. Cardiac troponin
956 T (cTnT) immunostaining of an auxin inducible degron strain of BRM (*Brm-AID*) at D10 of
957 differentiation induced with two different BMP4 concentration with or without IAA. **b**,
958 Immunostaining with cTnT shows that Brg1 loss is not rescued by addition of increasing amount
959 of BMP4. **c-e**, Heat maps showing differential enrichment of ATAC-seq peaks of WT and BRM
960 KO cells at D4 (**c**), D6(**d**) and D10 (**e**) of cardiac differentiation with normal (1x) and high (4x)
961 BMP4 concentrations. Boxed regions show restoration of WT-like chromatin in KO cells at high
962 BMP4 condition. Vertical lanes show replicate data. **f-g**, Browser tracks show chromatin
963 accessibility in WT and BRM KO cells along with H3K27ac marks in cardiomyocytes and neural
964 precursor cells (purple track) near indicated cardiac genes (**f**) and neural genes (**g**)
965



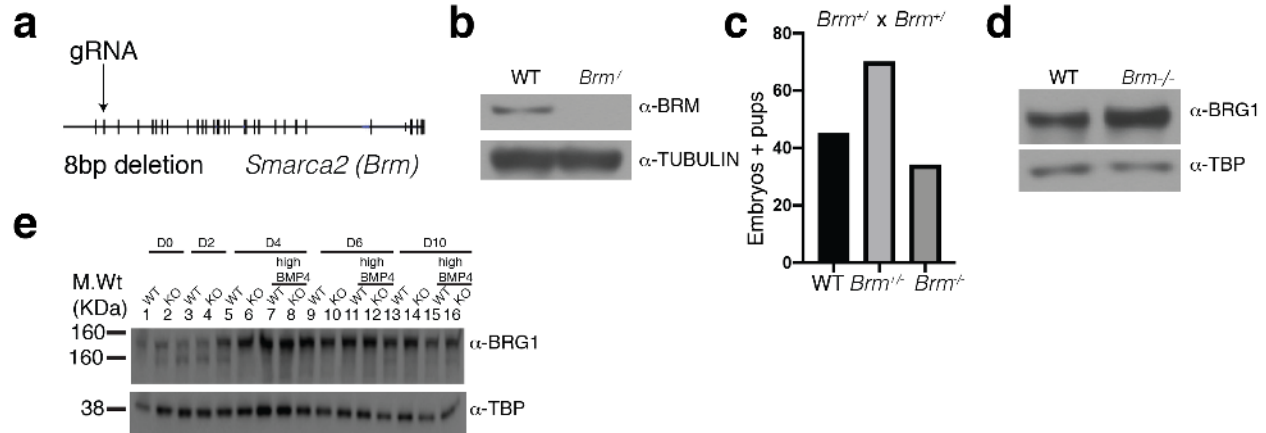
966
967

968 Extended Data Fig. 9. **BMP4 increases gene expression noise to restore WT-like gene**

969 **expression in *Brm*^{-/-} cells**

970 **a**, Dot plots showing quantitative changes in gene expression between WT and BRM KO cells
971 induced with normal (1x) or high (4x) BMP4 concentrations at D4, D6 and D10 stages of
972 differentiation for early developmental, cardiac mesoderm, precursors, myocytes and genes
973 enriched in BRM KO cells. **b**, Transcriptional trajectory analysis of WT and BRM KO cells in
974 presence of normal or high BMP4 concentrations showing the genotype representation (top)
975 and URD feature plots of expression of *Nkx2-5*, *Actc1* and *Otx2*. **c**, Western blots showing BMP
976 receptor, Smad1 and phosphor-SMAD expression during D0 to D4 of cardiac differentiation, **d**-
977 **e**, Scatter plots of single cell RNASeq data showing mean gene expression and variance from
978 mean gene expression at D4 stage of differentiation for WT (**d**) and BRM KO cells (**e**) in low and
979 high BMP4 conditions. **f-g**, Signaling entropy calculated similarly for WT (**f**) and BRM KO cells
980 (**g**) with low and high BMP4 conditions.

981
982
983
984
985
986
987
988
989
990
991
992
993
994
995



996
997

998 Extended Data Fig. 10. **BRG1 partially compensates for BRM loss *in-vivo***

999 **a**, The exon–intron organization of *Smarca2* (encodes BRM) and the site of guide RNA that
1000 targets exon2. The mouse strain from this transfection had an 8 bp deletion leading to
1001 premature stop codon. **b**, Western blot with anti-BRM antibody showing loss of BRM protein in
1002 *Brm*^{-/-} mouse brain whole cell extract. a-tubulin is used as a loading control. **c**, Heterozygous
1003 *Brm* mouse mating resulted in pups and embryos at a mendelian ratio. **d-e**, Western blot with
1004 antibody against BRG1 shows partial BRG1 compensation in absence of BRM in mouse brain
1005 (d), but no compensation in the in-vitro cardiac differentiation system (e).

1006